Boundary-Layer Transition Prediction Through Loose Coupling of OVERFLOW and LASTRAC

Balaji Shankar Venkatachari*
National Institute of Aerospace, Hampton, VA 23666

Jared A. Carnes†
University of Tennessee, Knoxville, TN 37996

Chau-Lyan Chang‡ and Meelan Choudhari§
NASA Langley Research Center, Hampton, VA 23681

Abstract

Transition prediction based on linear stability theory is expected to more accurately reflect the causality of transition onset than phenomenological transition models based on RANS-like transport equations. To help achieve the CFD Vision 2030 aim of building a CFD tool chain with automated prediction of boundary layer transition, a technique to loosely tie the NASA OVERFLOW CFD solver with the LASTRAC stability analysis tool is described. The coupled solver is then used to compute transition over a flat plate in a freestream with sufficiently low levels of turbulence, NLF(1)-0416 airfoil, the 6:1 prolate spheroid at an angle of attack, and a NASA juncture flow model with symmetric wing configuration. The findings for the 2D cases and the 6:1 prolate spheroid show that the loosely coupled approach is able to predict the transition location accurately in scenarios that are dominated by a single transition mechanism involving Tollmien-Schlichting instabilities, crossflow instabilities, or separation bubble-induced transition, or include a mixture of selected mechanisms. For the abovementioned cases, the toolset presented here appears to be robust to the prescription of the initial transition location, and it can lead to a converged solution in four or five rounds of the mean flow calculation and stability analysis, with minimal input from the user. However, significant work remains to be done in terms of identifying more accurate models for the transition zone and an optimal prescription for a dual N-factor criterion for 3D geometries in order to improve the robustness of this approach and to achieve a more thorough automation. The results presented here are initial steps toward achieving that goal.

Nomenclature

c	=	chord length (m)
C_f	=	skin-friction coefficient [nondimensional]
C_p	=	surface pressure coefficient [nondimensional]
f	=	disturbance frequency [Hz]
M	=	Mach number [nondimensional]
N	=	logarithmic amplification factor
$\overline{q}$	=	vector of base flow variables
$\tilde{q}$	=	vector of perturbation variables
$\hat{q}$	=	vector of amplitude variables
Re_c	=	Chord-based Reynolds number [nondimensional]
Re_L	=	Reynolds number based on spheroid length [nondimensional]
T	=	temperature [K]
Tu	=	freestream turbulence intensity [nondimensional]
(u,v,w)	=	streamwise, wall-normal, and spanwise velocity components [m s^{-1}]

*Sr. Research Engineer, Email: balaji.s.venkatachari@nasa.gov, Senior member, AIAA
† Graduate Research Assistant, Mechanical, Aerospace, and Biomedical Engineering, Email: jcarnes6@vols.utk.edu, Student Member, AIAA
‡ Distinguished Research Associate, Computational AeroSciences Branch, Email: chau-lyan.chang@nasa.gov, Associate Fellow, AIAA
§ Aerospace Technologist, Computational AeroSciences Branch, Email: m.m.choudhari@nasa.gov, Fellow, AIAA

(x, y, z) = Cartesian coordinates [m]
x/c = chordwise coordinate scaled by reference chord length [nondimensional]
y^+ = near wall grid spacing in wall units [nondimensional]
α = angle of attack [deg], streamwise wavenumber [m^{-1}]
β = spanwise wavenumber [m^{-1}]
γ = intermittency [nondimensional]
λ = spanwise wavelength, transition zone length [m]
ρ = density [kg m^{-3}]
σ = spatial growth rate [m^{-1}]
(ξ, η, ζ) = streamwise, wall-normal, and spanwise coordinates [m]

Subscripts

∞ = farfield reference state

Abbreviations
AFT = amplification factor transport
CF = crossflow
CFD = computational fluid dynamics
LM = Langtry-Menter
LST = linear stability theory
PSE = parabolized stability equations
RANS = Reynolds-averaged Navier-Stokes
SST = shear stress transport
TS = Tollmien-Schlichting

I. Introduction

Accurate prediction of viscous flows with laminar-to-turbulent boundary layer transition is important for many applications such as the design of natural laminar flow wings, unmanned aerial vehicles, and crewed reentry vehicles, given the push for safer and/or greener technologies in the arena of aerospace research. Therefore, the topic of laminar-to-turbulent boundary-layer transition research has been identified as a critical and pacing item for computational fluid dynamics (CFD) in the NASA CFD Vision 2030 [1] study. Direct numerical simulations, and wall-resolved (and to a limited extent, wall-modeled) large-eddy simulations continue to be the only approaches capable of simulating the complete set of physical processes up to the onset of transition and the subsequent breakdown of the laminar boundary layer into turbulent flow. However, these approaches remain impractical because of their excessive computational cost and the need for an accurate specification of the initial and boundary conditions required to capture the excitation of the flow instabilities responsible for transition. Adequate information about the external forcing is often unavailable from most wind-tunnel and flight tests.

Presently, a majority of the CFD computations are performed by using the computationally efficient Reynolds-averaged Navier-Stokes (RANS) models, under the assumption that the flow is turbulent everywhere. Thus, efforts to develop models that incorporate information about the transition process into the RANS framework have gained substantial ground in recent years [2–9]. These RANS-based models often require that only local information be used to model transition, instead of using detailed boundary-layer profiles or integral boundary-layer parameters. They achieve this by solving additional transport equations and use correlations that determine the onset of transition, making it easy to be implemented in modern unstructured grid-based CFD codes. However, it may be noted that most of the RANS-based transition models perform adequately only in limited flow regimes, as they often rely on correlations derived from limited experiments. The inherent averaging process employed within the RANS procedure makes it difficult to capture the development of the linear instabilities and their subsequent nonlinear growth and an eventual breakdown. Despite this limitation of the transport-equation-based transition models, they remain an attractive option because the vehicle performance is often characterized in terms of integral quantities such as force and moment coefficients or through pressure/skin-friction distribution; and capturing the overall

impact of transition on these integral quantities is more important than modeling the detailed physics of the transition to turbulence. In limited speed regimes, transition models based on RANS-like transport equations have been successful in modeling a range of transition scenarios such as those initiated via linear instabilities of the boundary layer flow as well as through bypass mechanisms related to finite amplitude disturbances.

The most widely used and reliable approaches for the prediction of transition onset locations in aircraft design computations are semiempirical correlations based on the linear stability theory (LST), such as the e^N method introduced by Smith and Gamberoni [10] and van Ingen [11] or the parabolized stability equations (PSE) [12]. The amplification of the dominant primary instabilities of the boundary layer flow developing in the low disturbance environment over aircraft wings at all speed regimes, such as the Tollmien-Schlichting (TS) waves and stationary/traveling crossflow vortices in subsonic and transonic flows can be accounted for using either LST or PSE. However, the application of these approaches toward a coupled computation of laminar, transitional, and fully turbulent parts of a flowfield requires sufficiently well-resolved boundary layer profiles in the laminar parts of the mean-flow computations. The stability-theory approach also entails an increased computational cost as well as complexity, suffers from a lack of robustness, and often requires advanced understanding of the transition physics and the hydrodynamic stability theory that typical CFD users may not possess. These restrictions are difficult to overcome in modern CFD codes, which rely upon massive parallelization and the use of unstructured grids [13] that are not compatible with the global dependence of the stability characteristics in one or more spatial directions. To overcome these shortcomings, surrogate models based on the laminar flow information provided by the flow solver [14–18] have been used in lieu of the direct computation of stability characteristics. ONERA and DLR have also developed tools [19–21] to perform LST-based automated transition predictions within their in-house CFD codes. A similar effort focused on laminar-to-turbulent optimization by coupling the CFD solver with both LST and PSE techniques and an adjoint-optimization framework has been pursued at the University of Michigan, as reported in the works by Shi et al. [22] and Halila et al. [23]. However, such approaches are tightly coupled to the data structure used within a specific CFD code, making operations such as the extraction of wall-normal profiles rather difficult and expensive in the context of a parallel computing framework and cannot be quickly ported to a different suite of codes.

Given a few unique capabilities amongst the NASA CFD tools, such as automated grid adaptation and adjoint based design, as well as those in the NASA LASTRAC stability software [24, 25], it would be beneficial to develop a tool suite for automated, CFD-integrated modeling of the transition process that can use any of the available CFD codes with LASTRAC via a common interface that will work with both structured and unstructured grid-based solvers. To that purpose, recent enhancements to LASTRAC [26] have centered on making the stability analysis tool more user-friendly and robust, owing to the development of PyLASTRAC, a Python-based interface tool set. This work follows up with an update on the progress of a CFD-integrated transition prediction tool based on a loose yet automatic coupling between LASTRAC and the structured overset grid compatible solver OVERFLOW [27]. Concurrently, a similar endeavor involving the coupling of the unstructured grid-based solver FUN3D and LASTRAC is being pursued [28]. Because OVERFLOW employs structured overset grids, the interface required to connect it to LASTRAC must be distinct from that required for FUN3D (with a few unique, additional, solver dependent steps). In addition, we describe other parts of the transition modeling method in this paper that were not covered in the work using the FUN3D solver [26], such as the use of a smooth intermittency function that characterizes the transition zone, as well as on the robustness of the convergence process, especially when the lack of a priori knowledge about transition leads to starting the CFD computation with either an excessively long laminar region or a severe underprediction of the laminar zone.

The scope of this paper includes a brief description of the process through which the coupling between the stability and CFD codes is achieved and the demonstration of that coupling for canonical test cases that include a flat plate under a variety of disturbance conditions involving sufficiently low freestream turbulence, the NLF-0416 airfoil at both large and intermediate chord Reynolds numbers, and fully 3D geometries such as the 6:1 aspect ratio prolate spheroid and a variant of the NASA juncture flow model with a symmetric wing configuration that recently underwent testing at the NASA Langley Research Center. The 2D flow configurations mentioned above feature two separate transition scenarios, namely, Tollmien-Schlichting instabilities of an attached boundary layer and/or a separation-bubble induced transition. In comparison, the 3D case also involves crossflow transition, presumably dominated by the stationary modes of crossflow instability. Most of these configurations allow the predictions from the loosely coupled approach to be compared against available experimental measurements, as well as with the predictions of other RANS-based transition models.

The paper is organized as follows. Section II provides the details of both CFD and stability solvers and the strategy for coupling the two, along with details about the implementation of the intermittency distribution function. Various test cases and a discussion of the results are reported in Section III. Finally, concluding remarks are provided in Section IV.

II.Flow Solver, Stability Analysis Tools and Coupling Strategy

The details of the various software tools and the approach to develop an integrated CFD-transition prediction tool chain are provided in this section.

A. OVERFLOW – CFD Solver

Version 2.3b of the NASA OVERFLOW code [27] is an implicit, structured, overset grid Navier-Stokes solver that is capable of computing both time-accurate and steady-state solutions via a variety of options for the spatial as well as temporal discretizations. RANS-based transition models available in OVERFLOW 2.3b include: (i) the two-equation Langtry-Menter transition model (LM2009) [4] based on the 2003 version of Menter's shear-stress transport (SST) RANS model, along with the modifications proposed by Langtry et al. [6] to account for crossflow induced transition (LM2015); (ii) Coder's [8, 9] 2017b version of the amplification factor transport (AFT2017b) equation-based model that uses the Spalart-Allmaras (SA) model; and (iii) the Medida-Baeder transition model [5], which is essentially a coupling of the two-equation Langtry-Menter transition model with the SA model. OVERFLOW also allows for performing computations with a specified laminar region (where the production of turbulence is turned off), and this feature is utilized in the present work.

B. LASTRAC-Based Stability Analysis Tool

LASTRAC has the capability to perform stability analysis using LST as well as PSE about a mean flow. In conventional, quasiparallel linear stability theory (LST), the assumption of a locally parallel boundary layer allows the streamwise derivative terms to be dropped from the linear disturbance equations and the wall-normal velocity can be set equal to zero. While the LST predictions should be satisfactory for the simple 2D cases, we also assess the PSE approach in the present work. In the PSE approach for general 3D flow configurations, both the streamwise and spanwise curvatures are also considered along with the nonparallel terms to allow a broader range of physical effects to be incorporated, enabling more accurate predictions of the instability evolution than the quasiparallel, LST approach.

The PSE approximation is based on isolating the rapid phase variations in the streamwise direction from the slow evolution of the disturbance mode shape due to the locally weak but potentially O(1) cumulative effects of the mean-flow nonparallelism and the surface curvature. The effects of instability wave propagation within a fully three-dimensional boundary layer can be evaluated via a parabolic integration along suitable trajectories such as mean-flow streamlines or group velocity lines associated with the disturbance(s) of interest. The variables (ξ, η, ζ) denote the streamwise, wall-normal, and spanwise directions in the nonorthogonal coordinates and (u,v,w) represent the corresponding velocity components. The density and temperature are denoted by ρ and T. The Cartesian coordinates are represented by (x, y, z), respectively. The vector of basic state fluid variables corresponds to $\overline{\boldsymbol{q}}(\xi, \eta, \zeta) = \left(\overline{\rho}, \overline{u}, \overline{v}, \overline{w}, \overline{T}\right)^T$. The perturbations to the basic state have the form

$$\tilde{\boldsymbol{q}}(\xi,\ \eta,\ \zeta, t) = \hat{\boldsymbol{q}}(\xi, \eta) exp\left[i\left(\int_{\xi_0}^{\xi} \alpha(\xi')d\xi' + \beta\zeta\ - \omega t\right)\right], \tag{1}$$

where the perturbation vector is $\tilde{\boldsymbol{q}}(\xi, \eta, \zeta, \mathrm{t}) = \left(\tilde{\rho}, \tilde{u}, \tilde{v}, \tilde{w}, \tilde{T}\right)^{\mathrm{T}}$ and $\hat{\boldsymbol{q}}(\xi, \eta, \zeta) = \left(\hat{\rho}, \hat{u}, \hat{v}, \hat{w}, \hat{T}\right)^T$ denotes the vector of amplitude functions. The streamwise and spanwise wave numbers are α and β, respectively, and ω is the angular frequency of the perturbation. The spanwise wavelength is defined as $\lambda = 2\pi/\beta$. The unknown, streamwise-varying wavenumber $\alpha(\xi)$ is determined in the course of the solution by imposing a normalization condition that renders uniqueness to the decomposition in Eq. (1) involving a slow variation of the amplitude functions $\hat{\boldsymbol{q}}(\xi, \eta, \zeta)$ in the streamwise direction, and the rapidly varying phase term $\exp\left[\mathrm{i}\int_{\xi_0}^{\xi} \alpha(\xi')d\xi'\right]$. Substituting Eq. (1) into the linearized Navier-Stokes equations and invoking the scale

separation argument to neglect higher-order terms involving a suitable subset of the viscous and/or streamwise derivative terms, one obtains the PSE in the form

$$\left(\mathbf{L} + \mathbf{M}\frac{\partial}{\partial \xi}\right)\widehat{\boldsymbol{q}}(\xi, \eta) = 0. \tag{2}$$

The entries of the coefficient matrices for **L** and **M** along with a more detailed description of the method can be found in the Refs. [12, 22, 23]. In this work, the PSE marching is performed along a preidentified streamline path along the surface. The nonparallel growth rate of the disturbances along a streamline for a selected pair of ω and β is given by

$$\sigma_{\mathrm{PSE}}(\xi, \omega, \beta) = -\Im(\alpha) + \frac{1}{2}\frac{\mathrm{d}\widehat{\mathrm{K}}}{\mathrm{d}\xi}, \tag{3}$$

where $\widehat{\mathrm{K}}$ denotes the norm of the disturbance kinetic energy. The onset of laminar-turbulent transition is estimated by using the logarithmic amplification ratio, the so-called *N*-factor, relative to the lower neutral branch location, $\xi = \xi_{lb}$, where a given disturbance first becomes unstable,

$$N(\omega, \beta) = -\int_{\xi_{lb}}^{\xi} \sigma(\xi', \omega, \beta) d\xi'. \tag{4}$$

Here, we assume that transition onset is likely to occur when a function of the envelope *N*-factors based on stationary crossflow instabilities (N_{CF}) and the Tollmien-Schlichting instability waves (N_{TS}) reaches a certain threshold.

C. OVERFLOW-LASTRAC Coupling Strategy

The OVERFLOW code allows the user to prescribe specified regions of laminar flow for any given geometric model via a PLOT3D function file using an input namelist. This capability is used in conjunction with the PyLASTRAC tool suite and some auxiliary codes and Python/linux shell scripts to develop a loose coupling between the OVERFLOW and LASTRAC codes. The resulting tool chain allows automated, CFD-integrated predictions of mixed laminar, transitional, and fully turbulent flows. The overall workflow is depicted in Fig. 1. The flow solver is initialized with a prescribed extent of laminar flow region, and the converged solution and the underlying grid are passed to the solver-independent interface module. The interface module converts the data into a format that is suitable for LASTRAC, including the extraction of wall-normal profiles and computing the disturbance trajectories in the form of inviscid streamlines along the surface. LASTRAC is then invoked to perform the stability computations along each of those trajectories and provide a surface distribution of the *N*-factor envelope. For TS instabilities, one may use either the critical TS *N*-factor corresponding to the disturbance environment of the boundary layer flow of interest or Mack's well-known correlation relating the disturbance levels in the facility to *N*-factor:

$$N_{\mathrm{crit,TS}} = -8.43 - 2.4\, ln\, (\frac{Tu(\%)}{100}) \tag{5}$$

to identify the transition onset location. In the case of three-dimensional boundary layers with nonzero crossflow (CF), a similar computation of another critical *N*-factor (roughness-based, possibly) is used as part of determining the transition onset location. In regions where both TS and CF instabilities are present, a suitable combined metric must be used to predict the transition onset location. When the predicted *N*-factor envelope does not reach the desired critical level within the domain of the imposed laminar flow, linear extrapolation (using an appropriate segment of the *N*-factor envelope) is used to estimate a potential transition onset location. If the extrapolated location extends beyond the geometry, e.g., downstream of the trailing edge of an airfoil, the newly imposed transition onset location is reset to be slightly upstream of the trailing edge. In case of the initial onset location being set too far upstream in the domain, there is the possibility of the stability analysis predicting a result indicating no growth in disturbances. In such a scenario, the newly imposed transition location is shifted substantially downstream—by about 75% of the distance between the previously imposed location and the end of the geometry.

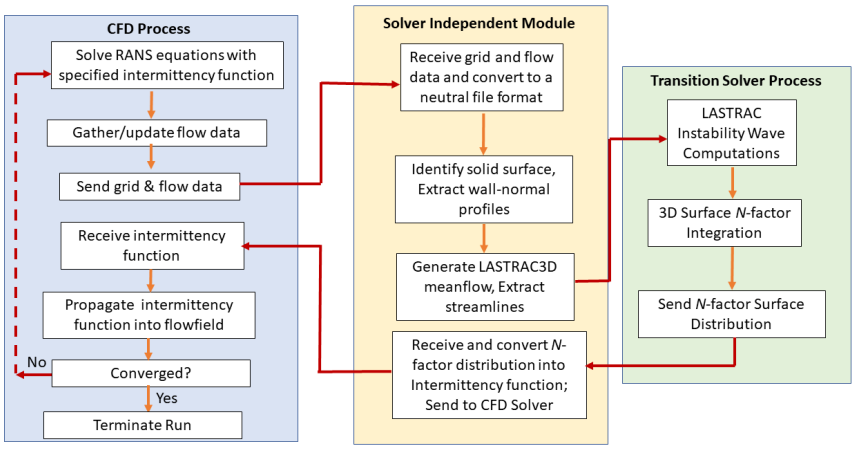

Fig. 1. Schematic of the coupling between OVERFLOW and LASTRAC.

To avoid large changes in the transition front across successive outer iterations and to improve the robustness of the iterative process outlined in Fig. 1, we underrelax the predicted transition onset location x_{tr}^{new} during the update to the imposed transition locations for the next run of the CFD solver, i.e.,

$$x_{tr}^{new} = x_{tr}^{old} + \theta(x_{tr}^{new} - x_{tr}^{old}) \tag{6}$$

where, θ is the relaxation parameter, and x_{tr}^{new} and x_{tr}^{old} correspond to the newly predicted and previously imposed transition locations, respectively. Usually, the underrelaxation parameter is set to a value between 0.7 and 0.9. However, in future, in lieu of using a fixed value of θ, one could easily switch to a dynamic procedure to set the underrelaxation parameter, wherein smaller values of θ are used at the start of the computation, when large changes may occur, and then, a gradual ramp up to higher values as the results approach convergence. The surface data and *N*-factor information are then converted into a smooth intermittency function, described below, to avoid a sharp transition from a laminar flow to a turbulent flow that could lead to a slower convergence of the CFD solver. In the present implementation, convergence is deemed to have been achieved if the shifts in the transition-onset location are within one or two grid points.

In the process outlined in Fig. 1, any CFD solver of choice can be used in the first box colored in blue, as long as it allows for the specification of laminar and turbulent regions in the flow and has a clean interface with explicit data-structure or allows for the reading of a surface/volume grid file of a specified format that contains markings for laminar and turbulent regions, through which the necessary information can be communicated. Most solvers can easily fulfil these constraints. Similarly, any other reduced-order stability analysis tools, such as those based on machine-learning algorithms [26, 29, 30], could be used to replace the LASTRAC stability solver in the green box from the schematic.

D. Intermittency Function

In the absence of a built-in transition model, CFD solvers often allow the user to impose a laminar region by switching off the turbulence production terms and/or the eddy viscosity within specified portion(s) of the grid. A binary coefficient is usually used to differentiate between purely laminar and fully turbulent subregions. A sudden transition of this type can cause an abrupt jump in the displacement thickness that are not physical and leads to difficulties in achieving convergence. Using an intermittency function, as proposed by Narasimha [31] would allow a more realistic modeling of the actual transition zone, as well as enabling a more robust convergence process. Based on measurements in 2D incompressible flows and additional assumptions about formation and breakdown of turbulent spots, Narasimha [31,32] had proposed an intermittency distribution function,

$$\gamma = \begin{cases} 0\,, & x < x_{tr} \\ 1 - \exp(-0.412\,\xi^2)\,, & x \geq x_{tr};\ \ \xi = \frac{(x - x_{tr})}{\lambda} \end{cases} \tag{7}$$

where x_{tr} is the onset location and λ is a distance parameter characterizing the length of the transition zone (usually defined as the distance between stations where $\gamma = 0.25$ and $\gamma = 0.75$ when experimental data on intermittency is available). There are other minor variants of this intermittency distribution function (see Ref. [32]). However, all of these expressions require an external determination of the key unknown in the form of the transition zone length λ. Candidate options to define this parameter have been proposed in Refs. [33-35], but those are restricted to flows without any rapid changes in the pressure gradient. The model proposed by Solomon et al. [36] is more general, also more complex. Therefore, based on limited experimentation, we introduce a simpler option that is easily related to the output from the stability solver. Specifically, we define the transition zone length to be the distance between the location where the *N*-factor envelope curve reaches the value of $0.8*N_{crit}$ (designated as $x_{tr,beg}$) and $1.1*N_{crit}$ or $1.2*N_{crit}$ (designated as $x_{tr,end}$). Note that the transition onset location x_{tr}, representative of where the skin friction coefficient rises from its laminar value in the actual flow, still corresponds to $N = N_{crit}$. However, the rise in skin friction from its laminar value lags behind the increase in the intermittency parameter, and hence, the location of intermittency rise, $x_{tr,beg}$, is defined to be upstream of the transition onset. After replacing x_{tr} in Eq. (7) with $x_{tr,beg}$ leads to the following expression for the intermittency function:

$$\gamma = \begin{cases} 0\,, & x < x_{tr,beg} \\ 1 - \exp(-0.412\,\xi^2)\,, & x \geq x_{tr,beg};\ \xi = \frac{(x - x_{tr,beg})}{(x_{tr,end} - x_{tr,beg})} \end{cases} \tag{8}$$

Currently, the same definition for the transition zone length is used for both TS instabilities as well for separation bubbles. Furthermore, this model does not lend itself to straightforward generalization when two different instability mechanisms are active simultaneously. Thus, there is considerable scope to improve upon this preliminary intermittency model.

III. Results and Discussion

The solutions presented here were obtained by running the OVERFLOW solver in steady-state mode using the 3rd-order Roe upwind scheme [37] and the unfactored successive symmetric overrelaxation (SSOR) implicit solution algorithm [38,39]. The CFD computation is based on the SA-neg-noft2 model (based on model nomenclature from the NASA turbulence modeling resource[**]) along with a specified laminar region. Each run of the CFD solver was carried out until the L2 norm of the mean flow residuals dropped by 8–10 orders before the stability analysis solver was invoked. To facilitate comparisons with the predictions based on the LST/PSE-based transition model, computations were also performed with the transport-equation-based transition models for some of the cases. In particular, the SA-based AFT2017b model and the SST-based LM2009 model were used for this comparison.

A. Flat Plate

As the first test case, subsonic flow over a two-dimensional zero-pressure-gradient flat plate with a sharp leading edge was computed for conditions that matched the experimental investigations by Schubauer and Skramstad [40] (also Schubauer and Klebanoff [41]), and those corresponding to the T3A- condition [42] from the T3 series of test cases hosted by the ERCOFTAC (European Research Community on Flow, Turbulence and Combustion). The freestream conditions and the turbulence intensity values used during the various runs are listed in Table 1. Freestream turbulence intensities from 0.03 percent to 0.875 percent at the plate leading edge are included in these computations. The Reynolds number range for the transition zone at each condition from the Schubauer and Skramstadt experiment [40] was also available for the low turbulent intensity cases, while limited skin-friction coefficient data was available for the T3A – case, and these data will be used for the assessment of both transition onset predictions based on the *N*-factor criterion and transition zone predictions based on the intermittency distribution function from Eq. (8).

[**] https://turbmodels.larc.nasa.gov

Table 1: Flow conditions for the flat plate test cases at the plate leading edge.

Case	Tu at the leading edge (%)	Freestream Velocity (m/s)	Density (kg/m^3)	Freestream Temperature (K)
Schubauer and Skramstad [40]; Schubauer and Klebanoff [41];	0.03, 0.125, 0.18, 0.3	50.1	1.2	288.17
ERCOFTAC T3A- [42]	0.875	19.8	1.2	288.17

The computational domain begins 0.15 m upstream of the flat plate leading edge and extends across a plate length of 2.5 m. The top boundary is located 0.3 m from the flat plate. The boundary conditions used are the following: nozzle inlet condition with specified total pressure corresponding to the freestream Mach number at the inlet, a Riemann characteristic top boundary, a constant-pressure boundary condition ($\frac{P}{P_\infty} = 1.0$) outflow, symmetry on the bottom boundary upstream of the flat-plate leading edge and viscous, adiabatic walls on the plate. The baseline grid (designated as the medium mesh) contained 721 points in the streamwise direction (including 193 points in the symmetry plane ahead of the leading edge) and 385 points in the wall-normal direction. The wall-normal spacing for the first grid point away from the wall was 4 x 10^{-6} m, corresponding to $y^+ < 0.5$ (estimated based on the flat plate boundary-layer theory at the transition onset location) for all conditions. In the immediate vicinity of the leading edge, this estimate is not expected to hold. Furthermore, the grid was designed to contain at least 100 points within the boundary layer, and the grid expansion ratio in the near-wall region was less than 1.03. In addition to the baseline mesh, a coarser mesh obtained by uniform coarsening of the baseline mesh by a factor of 2/3 (overall size: 481 x 257), and a finer mesh (961 x 513) obtained by uniform refinement factor of 4/3 were also employed for a grid independence study.

Mack's correlation from Eq. (5) was used to determine the critical TS *N*-factor for all flat plate cases with a turbulence intensity (Tu) greater than or equal to 0.125%. In the experiments by Schubauer and Skramstad [40], it was observed that the transition Reynolds number remained constant for $Tu < 0.07\%$, and was probably controlled by the wind-tunnel acoustics. Moreover, as mentioned by Crouch [43], Mack's correlation yields good results only when $Tu > 0.07\%$ and is expected to hold up to Tu =2.0%. Hence, for the single case with Tu = 0.03%, the N_{crit} parameter was set to a value of 7.6, as it corresponded to a transition location that matched well against the data from the experiment. Incidentally, if one were to use Mack's correlation, the critical *N*-factor of of N_{crit} = 7.6 corresponds to Tu = 0.125%. Based on the abovementioned finding of Crouch [43], it is questionable whether Mack's correlation would apply to the T3A- case with a freestream turbulence intensity of Tu = 0.875%, which is likely to fall within the range of bypass transition and we investigate that question here.

In Fig. 2, the iterative convergence of the streamwise evolution of the skin-friction coefficient is shown for the case with Tu = 0.18%. In this case, the initial transition location during Run 1 was set at x = 1.009 (Re_x ~ 3.39 x 10^6). From Fig. 2, it can be observed that the transition location has converged visually by iteration 3 of the combined set of computations comprised of a CFD run followed by the stability analysis, with the transition region falling within the range of measurements obtained during the experiment of Schubauer and Skramstad [40]. As mentioned in Section II D, the definition of the transition zone length is an important parameter in the definition of the intermittency function. Figure 3 illustrates the influence of the choice for the $x_{tr,end}$ parameter (while the other parameter, $x_{tr,beg}$, is held fixed) on the evolution of the intermittency distribution function and the streamwise distribution of the skin-friction coefficient. In this case, $x_{tr,end}$ was determined to be the location where the *N*-factor envelope reaches a value of either 1.1*N_{crit} or 1.2*N_{crit}, and $x_{tr,beg}$ is held fixed at the location where a value of 0.8*N_{crit} is reached. By choosing the $x_{tr,end}$ location to coincide with the station where an *N*-factor of 1.1*N_{crit} is reached, one obtains a shorter transition zone in comparison with that obtained by associating $x_{tr,end}$ with the location where an *N*-factor

of 1.2*N_{crit} is reached, as well as in a sharper rise in C_f. Furthermore, the start of the transition zone appears to shift slightly upstream with the choice of $x_{tr,end}$ =1.1*N_{crit}. Also, as previously mentioned in Section II.D, the lag between the rise of the intermittency function and where the skin-friction coefficient first departs from the laminar behavior is clear from this plot. This lag occurs because the RANS-based models require a finite distance before the effects of the nonzero turbulence production can cause the skin-friction coefficient to depart from its laminar value. Based on Fig. 3, an intermittency value of about 0.2 seems to roughly correspond to the location where the C_f starts to rise. Of course, in the future, it may be possible to change the intermittency function model to ensure that the place where C_f begins to climb coincides with the location in the N-factor envelope where a value of N_{crit} is reached. Computations were performed for three different meshes with progressively finer resolution, with an identical value of initial guess for the transition location in each case. The skin-friction distributions corresponding to the converged solution from the iterative process of N-factor-based transition calculation on each mesh are shown in Fig. 4. For the curves shown in this plot, the transition zone length in the intermittency distribution function was defined using $x_{tr,beg} = 0.8 * N_{\mathrm{crit}}$ and $x_{tr,end} = 1.1 * N_{\mathrm{crit}}$. Given that the skin-friction curves for the different meshes are indistinguishable, and the predicted transition region aligns well within the experimentally measured transition region, one may conclude that the results are grid converged, and furthermore, that the coupling process is robust as desired.

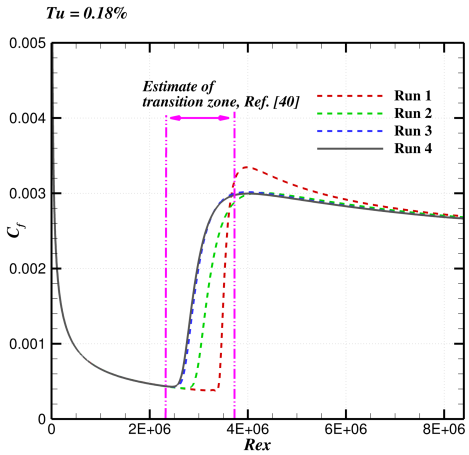

Fig. 2. Iterative evolution of the skin-friction coefficient distribution for the flat plate case with *Tu* = 0.18%. The magenta lines indicate the onset and end of transition based on surface fluctuation measurements by Schubauer and Skramstad [40].

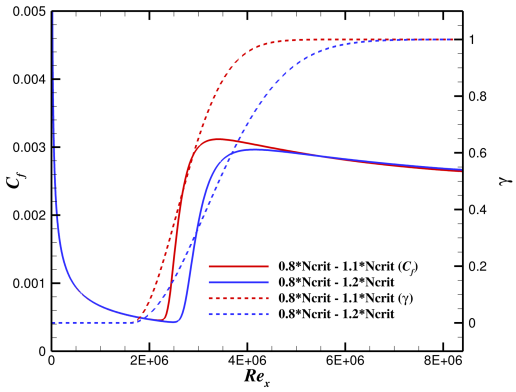

Fig. 3. Evolution of the skin-friction coefficient distribution (solid lines) and the intermittency function (dashed lines) for different specifications of transition region length in the intermittency function for the flat plate case with *Tu* = 0.18%.

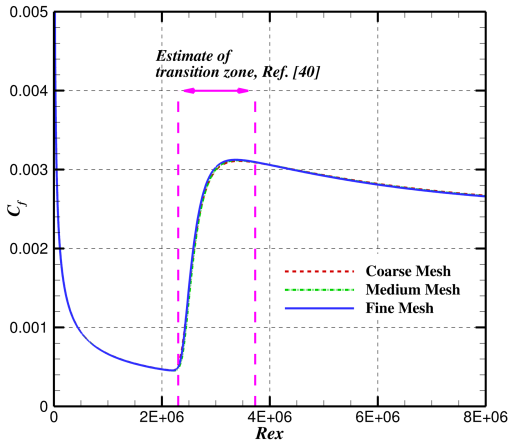

Fig. 4. Comparison of skin-friction coefficient distribution for different mesh resolutions, for the flat plate case with *Tu* = 0.18%.

In Fig. 5, an overall summary of the results obtained using the OVEFLOW-LASTRAC coupling approach for the various turbulence levels investigated here and their comparisons with the measured data from the experiment of Schubauer and Skramstad [40] is provided. Also, the comparison between the red square symbols and green triangles in this plot illustrates the influence of choosing different definitions for the transition zone length in the intermittency distribution function. Additionally, the solid blue line in this plot corresponds to a best-fit curve provided in Schubauer and Skramstad [40] for the data from the experiment, while the black dash-dot-dot line is the transition onset obtained for different freestream turbulence levels by Crouch [43] using stability analysis and Mack's correlation. Also, the reader is reminded that in the plot, the data corresponding to Tu = 0.03% and 0.125 % are the same as we use the same N_{crit} for both the conditions. For $Tu \leq 0.18\%$, the choice of $x_{tr,end} = 1.1 * N_{\text{crit}}$ (which corresponds to a smaller length of the transition zone) provides a better match with the experimental data, whereas choosing the higher value of $x_{tr,end} = 1.2 * N_{\text{crit}}$ (i.e., the larger extent of transition zone) results in a downstream shift in the overall transition zone in comparison with the measurements. For $Tu > 0.18\%$, choosing $x_{tr,end} = 1.1 * N_{\text{crit}}$ again leads to a good match for the start of the transition zone, but the transition zone ends slightly upstream of the measured location. On the other hand, for $x_{tr,end} = 1.2 * N_{\text{crit}}$, the start of the transition zone is slightly downstream of the measured location, but the end of the transition zone seems to be closer to the measured locations. One option that we did not explore as part of this work, was to retain $x_{tr,end} = 1.2 * N_{\text{crit}}$ but shift $x_{tr,beg}$ slightly upstream and this will be investigated as part of the future refinements. Overall, the present set of results indicate that our initial guess for the intermittency distribution function yields reasonable results, at least from the perspective of a flat plate case, and the match with the data from Crouch [43] provides additional validation of the LASTRAC stability results based on the velocity profiles obtained from OVERFLOW computations. Furthermore, using this data in conjunction with additional measurements related to flows with favorable and adverse pressure gradients would help better optimize the parameters used in the definition of the intermittency distribution function.

.

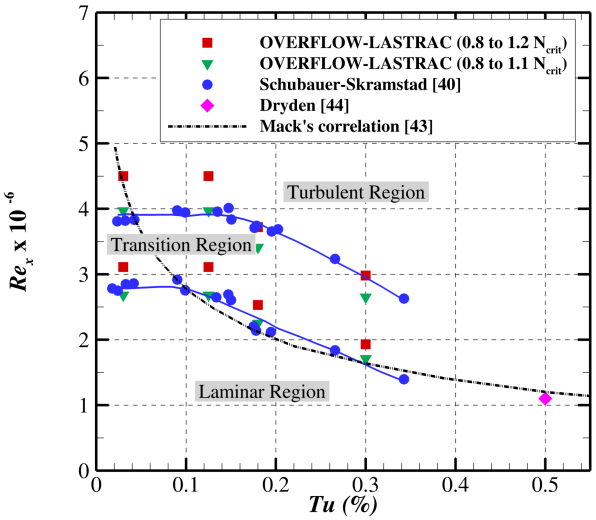

Fig. 5. Effect of turbulence and the specification of transition region length in the imposed intermittency function on the transition Reynolds number for the flat plate case and its comparison against experimental data from Schubauer and Skramstad [40].

In Fig. 6(a), iterative convergence of the skin-friction coefficient is shown for the T3A- condition (Tu = 0.87% at the leading edge). As seen from this plot, by the third iteration of the mean flow computation and stability analysis cycle, the results have already converged, such that the skin-friction curves obtained from the fourth and fifth iterations are visually indistinguishable from those obtained after the third iteration. However, the converged results indicate the start and end of transition zones to be significantly upstream of the measured data, with a large error of nearly 50% in terms of Re_x. If the Schubauer and Skramstad data in Fig. 5 were to be extrapolated to Tu = 0.87%, one would not expect to see transition onset at the relatively high Reynolds number of $Re_x \approx 1.7 \times 10^6$ as measured during the T3A- experiment. One of the reasons for this later onset of transition during the experiment is that the freestream turbulence intensity decays along the length of the plate. The measured turbulence intensity at the transition location corresponds to Tu = 0.47%, whereas the critical N-factor used for the transition prediction is based on extrapolating Mack's correlation to the leading-edge value of Tu = 0.87%. In this case, it will be hard to match the experimental transition without a receptivity model for the excitation of T-S waves via freestream turbulence. However, even after using the lowest value of freestream turbulence directly at the transition location (namely, Tu = 0.47%), the predicted transition location is still upstream of the measured value as seen from Fig. 6(b). This finding clearly supports the hypothesis that the underlying physics of the transition process during the T3A- experiment was rather different from that in the Schubauer and Skramstad experiment. As further confirmation, we have included an additional plot in Fig. 7 below, which augments the dataset from Fig. 5 with additional data points based on the ERCOFTAC T3 series of experiments [42]. Shown in Fig. 7 are the locations of the transition onset and end of transition, based on the skin-friction data and the freestream turbulence intensity measured at the leading edge. Data shown correspond to conditions T3A- as well as for the bypass transition cases designated as T3A (Tu = 3.3%) and T3B (Tu = 6.5%), respectively. Given the substantial decay in turbulence intensity from the leading edge to the location of transition onset in the T3 experiments, the same data are also plotted against freestream turbulence intensity measured at the transition onset location. Figure 7 also includes a linear curve fit through these additional data points from the T3 test series. The trend shown for the T3 series of data, is very different from the trend based on the Schubauer and Skramstad [40] data, clearly indicating that the T3 series of experiments belongs to a different (i.e., bypass) branch of transition scenario as opposed to the TS dominated transition. Hence, we will not be able to predict it using an approach based on a stability analysis.

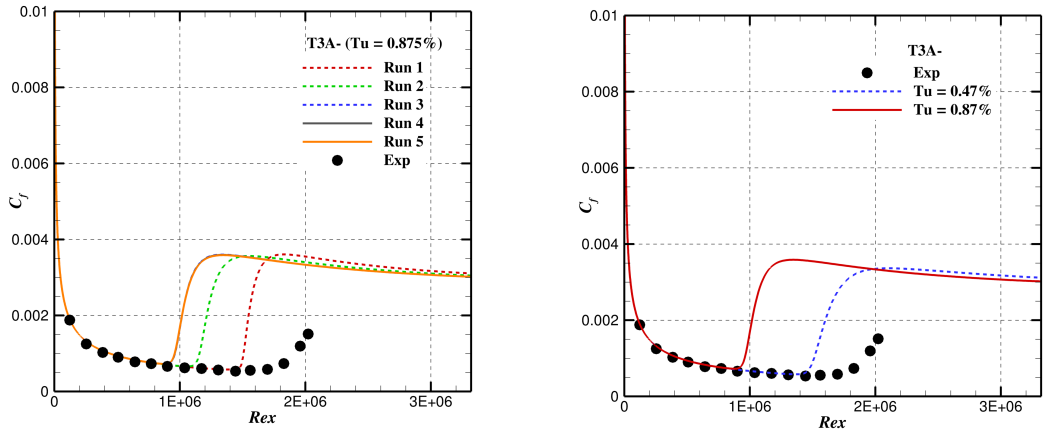

(a) Iterative convergence **(b) Influence of *Tu***

Fig. 6. Iterative evolution of the skin-friction coefficient distribution for the T3A- case and its sensitivity to the chosen freestream turbulence intensity for determining the N_{crit} for transition prediction based on stability analysis.

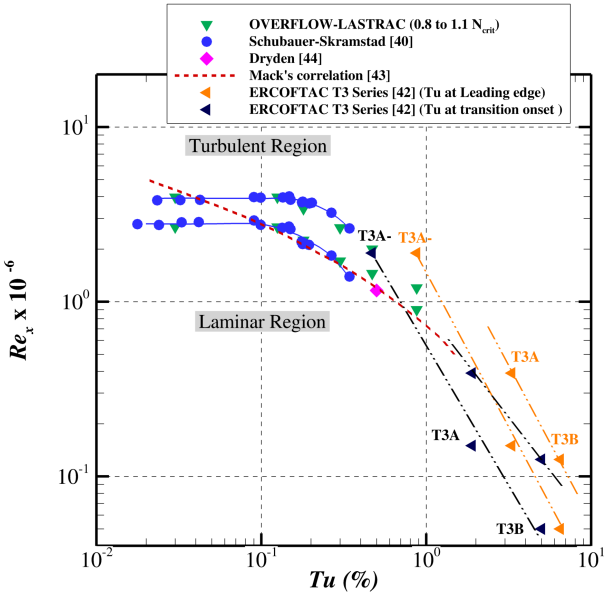

Fig. 7. Effect of turbulence the transition Reynolds number for the flat plate case and its comparison against experimental data from Schubauer and Skramstad [40] and from the T3 series [42].

B. Natural Laminar Flow Airfoil, NLF(1)-0416 — Low Reynolds Number Case

The NLF(1)-0416 airfoil is a natural laminar flow configuration that was developed at the NASA Langley Research Center by D. Somers. It is designed for general aviation applications to achieve a high value of the maximum lift coefficient and a low cruise drag coefficient. Reference [29] provides further information on the geometry and experimental test conditions, as well as the measured results. The flow condition studied herein corresponds to $M_\infty = 0.1, Re_c = 4 \times 10^6$, $c = 1$ m, $\alpha = 0°$ and $5°$, and $T_\infty = 300$ K, as specified for the AIAA Transition Modeling and Prediction workshop.[††] The freestream turbulence intensity in the experiment was 0.15%. Accordingly, we used the critical *N*-factor of 7.2 to predict the onset

[††] https://transitionmodeling.larc.nasa.gov/wp-content/uploads/sites/109/2020/02/TransitionMPW_CaseDescriptions.pdf

of transition. The same intermittency distribution function used for the flat plate case was invoked here, namely, with a transition zone defined on the basis of $x_{tr,beg} = 0.8 * N_{\text{crit}}$ and $x_{tr,end} = 1.1 * N_{\text{crit}}$. At the zero degree angle of attack, the onset of transition is triggered by TS instabilities on the upper and lower surfaces of the airfoil. At $\alpha = 5°$, transition is triggered by TS instabilities on the upper surface of the airfoil, whereas transition on the lower surface is induced by a laminar separation bubble. The results presented here were obtained using the extra-fine C-grid provided by the AIAA Transition Modeling and Prediction workshop committee and contained 1025 points around the airfoil (along with 193 points in the wake region) and 193 points in the wall normal direction, with a nondimensional near-wall spacing of $y^+ \sim 0.2$ (estimated based on the flat plate boundary-layer theory at the midchord location). Additional computations on a coarser grid (designated as the fine grid by the workshop committee) and a finer grid (designated as the ultrafine grid), confirmed that the results were nearly insensitive to the level of grid resolution.

In Figure 8, we show the iterative evolution of the skin-friction coefficient, C_f, for the 0° angle of attack condition after each outer iteration of the CFD runs for a specified transition location. For the initial run, the imposed transition location was close to the final, converged transition front on the upper surface, while it was downstream by about 6% chord length from the final location on the lower surface. After the third round of outer iterations, both the solution and the transition location appear to have visually converged on both sides of the airfoil. As displayed in Fig. 9(a), the pressure coefficient distributions from the integrated, stability-based model and the two transport-equation-based transition models match well with each other and with the measured data from the experiment, apart from minor differences in the immediate vicinity of the transition location. The comparison of skin-friction distributions from the three different models is shown in Fig. 9(b) along with a region marked by a grey-colored box indicating where flow switched from being laminar to turbulent in the experiment. The plot indicates that the predicted transition onset location from the loosely coupled, stability-based model matches well with the LM2009 prediction, and that from the experiment, while differing slightly from the prediction based on the AFT model.

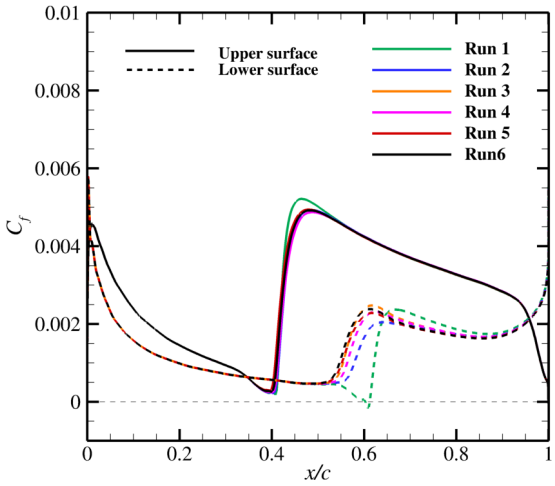

Fig. 8. Iterative evolution of skin-friction coefficient distribution over NLF(1)-0416 airfoil.

The results for $\alpha = 5°$ are shown in Figs. 10–12. Downstream of the suction on the upper surface of the airfoil, the boundary layer experiences an adverse pressure gradient, whereas the lower surface boundary layer develops under a favorable pressure up to 60% chord before encountering an adverse pressure gradient (see Fig.11(a)). Because transition on the lower surface is triggered by the laminar separation bubble at this flow condition, we tested two variations in the initial position of imposed transition in order to test the robustness of the automated process. In Fig. 10, we show the results for the case where the initial position of the imposed transition location is placed at the midchord location on the upper surface and delayed until 80% chord on the lower surface. For both surfaces, these imposed transition locations are downstream of the final location, and therefore, there was sufficient laminar region to perform the stability analysis. Within three iterations of the mean flow computation, stability analysis, and updates to imposed transition location, the solution on the lower surface was practically converged, but one more iteration was necessary to achieve convergence on the upper surface.

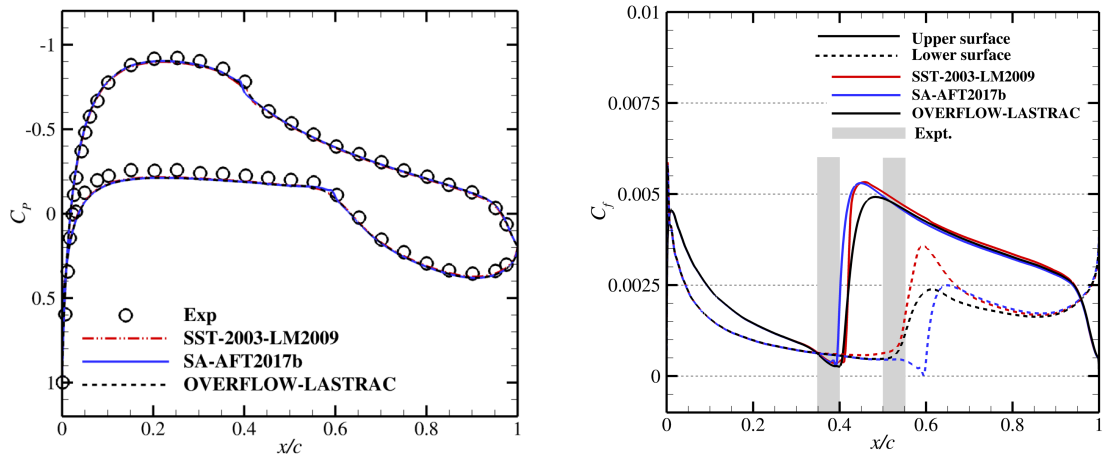

(a) Pressure coefficient **(b) Skin-friction coefficient**

Fig. 9. Pressure coefficient and skin-friction distribution for NLF(1)-0416 airfoil at $\mathbf{Re_c = 4\,x\,10^6}$, and $\boldsymbol{\alpha = 0°}$.

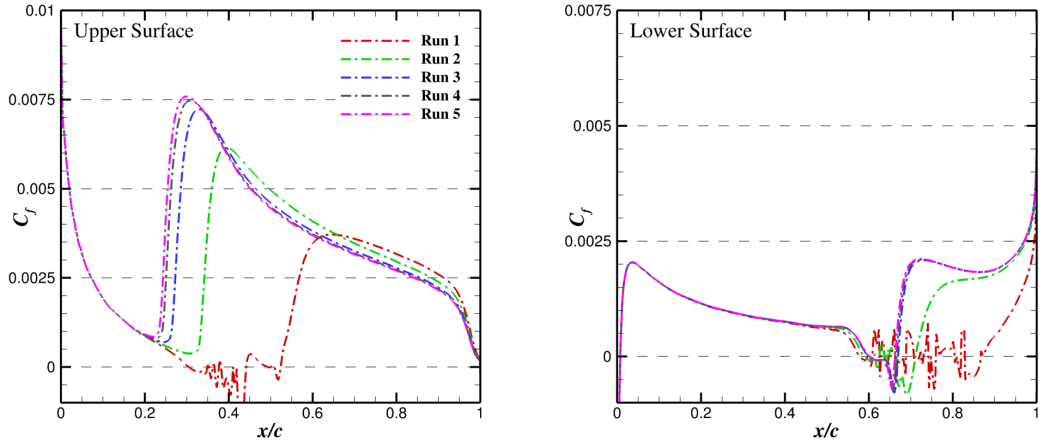

Fig. 10. Iterative evolution of skin-friction coefficient distribution on the upper and lower surfaces of the NLF(1)-0416 airfoil at $\mathbf{Re_c = 4\,x\,10^6}$, and $\boldsymbol{\alpha = 5°}$. The initial transition location was set downstream of the exact location on both the upper and lower surfaces.

The resulting pressure coefficient distributions from the integrated, stability-based model and the two transport-equation-based transition models match well with each other and with the measured data from the experiment as shown in Fig. 11(a). The converged locations of the beginning of transition also compares favorably with the predictions based on both LM2009 and AFT models, as one may observe from the skin-friction distributions plotted in Fig. 11(b). No measurements of the transition zone on the upper surface are available from the experiment, but such measurements were available on the lower surface (indicated by a grey-colored box in Fig. 11(b)) and the comparison with those measurements indicates that the integrated, stability-based model predicts the start of the separation bubble correctly, but the reattachment appears to happen downstream of both the measured transition location and the transition locations predicted by the transport-equation-based transition models. Note that the same intermittency distribution function used for the flat plate case was invoked here, namely, with a transition zone defined on the basis of $x_{tr,beg} = 0.8 * N_{\text{crit}}$ and $x_{tr,end} = 1.1 * N_{\text{crit}}$. As indicated in Section II-D, ideally, the definition of the transition zone length in the case of separation bubble should be different from that used for the TS instabilities. Thus, the larger bubble length predicted here could be improved by using wind tunnel data for additional separation bubble configurations. As part of future work, we plan to explore alternative definitions of the transition zone length for the case of separation bubbles.

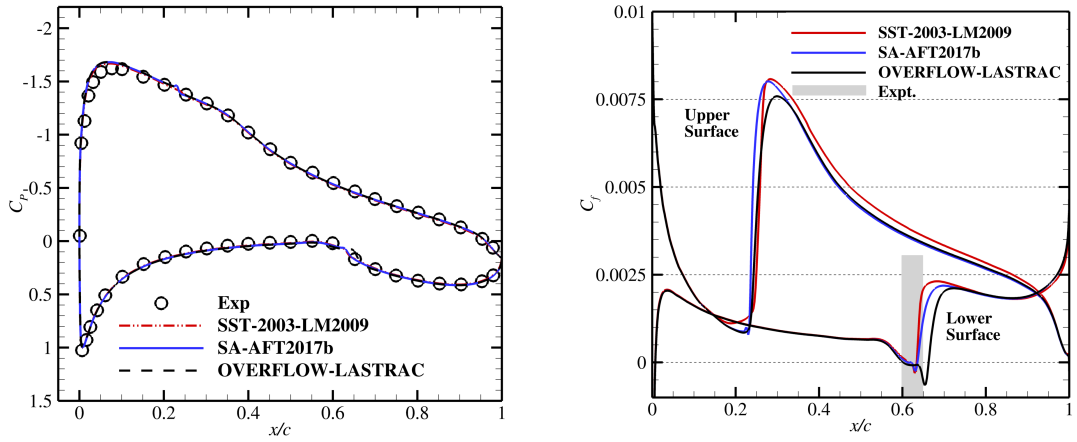

(a) Pressure coefficient **(b) Skin-friction coefficient**

Fig. 11. Pressure coefficient and skin-friction distribution for NLF(1)-0416 airfoil at $\mathrm{Re}_c = 4 \times 10^6$, and $\alpha = 5°$.

In Fig. 12, we show the iterative evolution of C_f distribution for the case where the initial position of the imposed transition location on the upper surface is once again at the midchord location, but the initial transition location on the lower surface is moved to a location near the 40% chord location, i.e., significantly upstream of the measured transition location. As the initially imposed transition location was significantly upstream on the lower surface, stability analysis performed after the initial run predicted no growth in disturbances within the available region, initiating the automation script to shift the imposed transition location downstream, closer to the trailing edge. After that, within another two iterations, the process resulted in converged results for both the upper and lower surfaces, indicating the robustness of the automated process. The final distributions of surface pressure and skin-friction coefficient were found to be the same as those predicted during the previous set of runs discussed in the case of Fig. 10 and shown in Fig. 11.

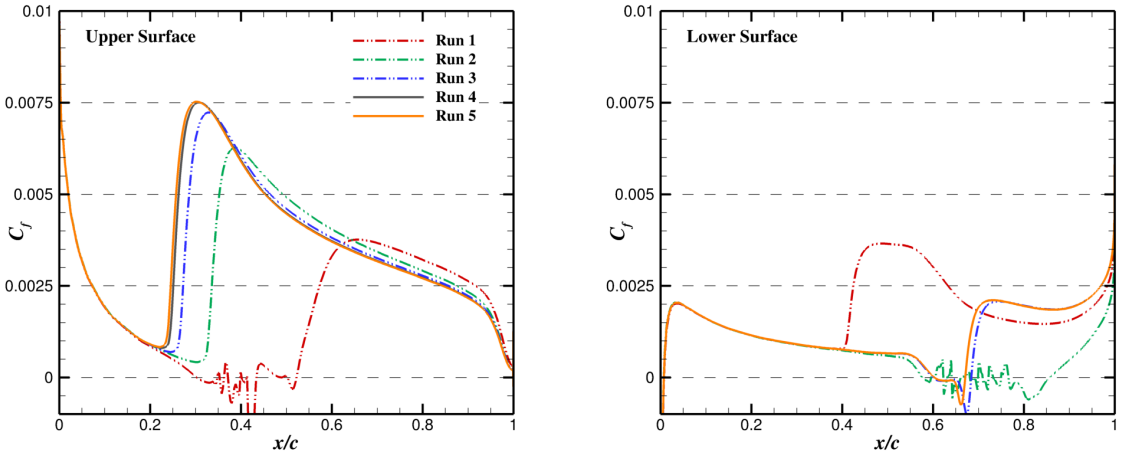

Fig. 12. Iterative evolution of skin-friction coefficient distribution on the upper and lower surfaces of the NLF(1)-0416 airfoil at $\mathrm{Re}_c = 4 \times 10^6$, and $\alpha = 5°$. The initial transition location was set downstream of the exact location on the upper surface, while it was set upstream of the exact location on the lower surface.

C. NLF(1)-0416 —High Reynolds Number Case

To test a flow condition where the onset of transition is purely due to T-S instabilities on both sides, the airfoil computation was repeated for a higher Reynolds number condition with $\mathrm{Re}_c = 9 \times 10^6$, while the other flow parameters remained fixed at $M_\infty = 0.1, c = 1\ \mathrm{m}, \alpha = 0°$, and $T_\infty = 300\ \mathrm{K}$. The earlier computational grid was designed to provide an adequate spatial resolution even at this higher Reynolds

number; hence, the same grid was used in this case. The critical *N*-factor for transition onset was also held fixed at 7.2. Table 2 shows the converged transition locations on either surface of the airfoil as obtained from the loosely coupled, stability-based model and their comparison with the results obtained with the AFT2017b and LM2009 models. As observed in the earlier cases, the results converged after three-to-four cycles of the mean flow computation, stability analysis and updates to imposed transition location. For the lower surface, the transition location predicted by the loosely coupled model is bracketed by the predictions based on the AFT2017b and LM2009 models, respectively, while the predicted transition location on the upper surface is downstream of the locations predicted by both LM2009 and AFT models. Consistent with the increase in Reynolds number relative to the case in subsection B (see Fig. 9(b)), the predicted transition location in the present case is upstream of both the predicted and the measured transition locations at the lower Reynolds number of $\mathrm{Re}_c = 4 \times 10^6$. Also, as discussed in section II-B, for simple 2D geometries, LST and PSE should yield similar results that can be seen from Fig. 13, where the *N*-factor envelopes predicted by LASTRAC using LST and PSE, respectively, are shown after the initial run of the CFD solver. Highlighted in the plot are the locations where the envelope *N*-factors based on both LST and PSE and the upper as well as the lower surface exceed the critical value of *N*-factor.

Table 2. Predicted transition location for the NLF(1)-0416 airfoil at $\mathrm{Re}_c = 9 \times 10^6$, and $\alpha = 0°$, along with the corresponding predictions from the RANS-based transition models.

	x_{tr}^{upper}/c	x_{tr}^{lower}/c
OVERFLOW-LASTRAC	0.330	0.328
LM2009	0.275	0.300
AFT2017b	0.316	0.352

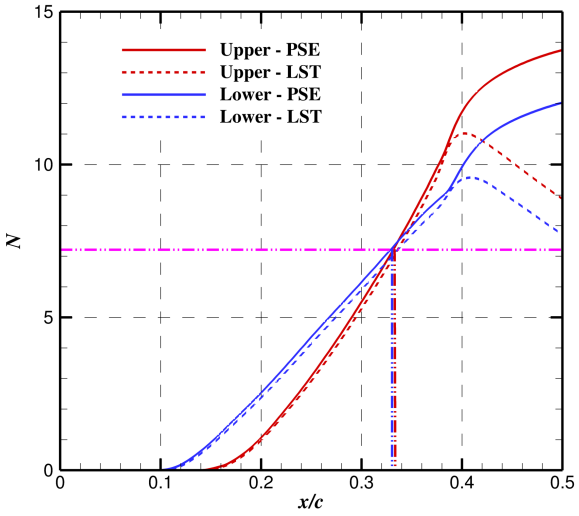

Fig. 13. *N*-factor envelope computed with LASTRAC using both PSE and LST with the basic state computation for the NLF(1)-0416 airfoil at $\mathrm{Re}_c = 9 \times 10^6$, and $\alpha = 0°$.

D. 6:1 Prolate Spheroid

As the first 3D case, we consider the subsonic flow over a 6:1 prolate spheroid that was experimentally studied by Kreplin et al. [46], given that it is representative of a simplified fuselage of a transport aircraft. For this geometry, transition can happen via TS waves and/or CF instability based on the Reynolds number and angle of attack, and has become the focus of many transition prediction workshops, including the AIAA Transition Modeling and Prediction workshop and the NATO AVT-313 Incompressible Flow Transition Comparison Workshop. Previously, Spall and Malik [47], Stock [48], and Krimmelbein et al. [48] have reported stability analysis of the boundary layer flow on this geometry. The flow condition considered in the present work corresponds to an angle of attack of 10°, a freestream Mach number of 0.136, and freestream

temperature 300 K. The Reynolds number based on the spheroid length (L=2.4 m) was 6.5 × 10^6. A multi-block structured grid was used to avoid a singularity along the major axis of the model near the nose and at the aft end of the geometry. The central portion of the grid had a size of 481 × 289 × 385 points along the streamwise, azimuthal, and wall-normal directions, respectively, whereas each of the nose and the aft blocks had a size 97 × 97 × 385. The first grid point away from the surface was located at $\frac{\Delta y}{L} = 1.0 \times 10^{-6}$, with y^+ ~ 0.25 (based on the location $x = L$). The grid was designed to contain at least 100 points within the boundary layer. The outer domain was placed 100 spheroid lengths away from the body.

For this case, no intermittency distribution function was used due to ambiguities regarding how it should be formulated for a case with both TS and CF instabilities playing a role. Also, due to time constraints, we carried out only two iterations of the CFD run–stability analysis cycle, without use of underrelaxation and hence these results need to be considered as being preliminary. In Figure 14(a), the skin-friction contours obtained from the experiment are shown in a rolled-out configuration (streamwise length vs. azimuthal angle) along with the inferred transition location. Also shown in Fig. 14(b) are the skin-friction contours obtained using OVERFLOW after the initial run, when the transition was arbitrarily enforced at x/L = 0.7 and that obtained after imposing the transition locations based on stability analysis computations performed based on the initial run. With the imposed front getting closer to the inferred front from the experiment, one can observe that the skin-friction contours from CFD agree well with that from the experiment, with the exception being that the maximum skin-fricition coefficient obtained in the CFD are currently slightly lower than that from the experiment. Additional iterations of the loosely coupled solver will be run and reported in a future publication.

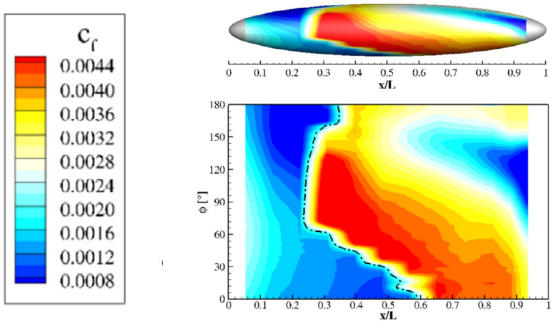

(a) Experiment

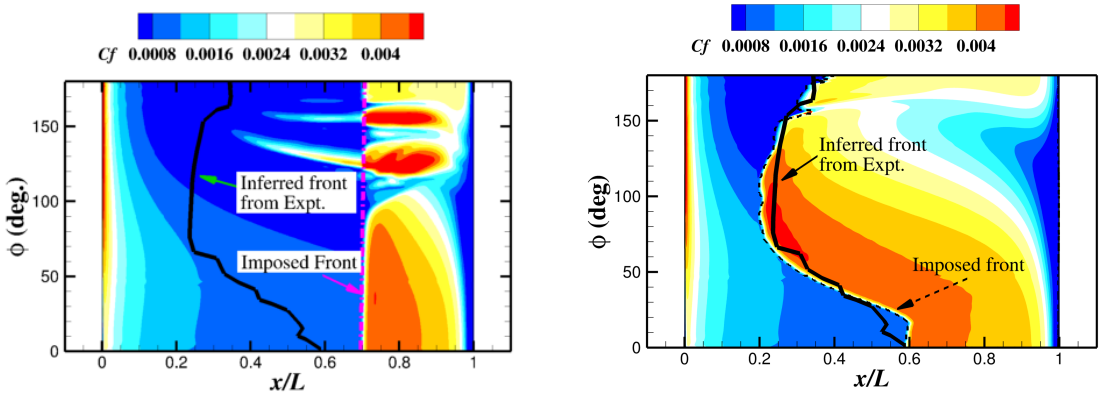

CFD Iteration 1 **CFD Iteration 2**

(b) Skin friction contours for the basic state obtained with OVERFLOW with different imposed transition fronts.

Fig. 14. Skin-friction contours on the 6:1 prolate spheroid for Re_L = 6.5 x 10^6 and α = 10° obtained from the experiment as well as from two different basic states from CFD with different imposed transition locations.

To perform the PSE analysis for this problem, the spheroid was seeded with 65 seed points equally distributed along the azimuth direction and is shown in Fig. 15. With the PyLASTRAC tool suite, one has the ability to automatically generate the streamlines needed for performing the stability analysis through random seed generation. However, we did not use that feature here, in order to facilitate potential troubleshooting during this initial evaluation stage of the automated tool chain.

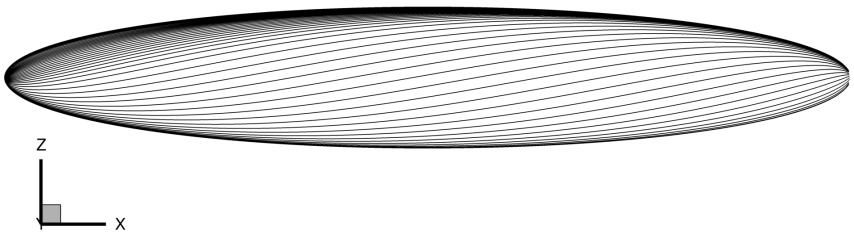

Fig. 15. Streamlines used for PSE with LASTRAC.

The TS and CF *N*-factor contours obtained via PSE computations after the initial run are shown in Figs. 16(a) and 16(b), respectively. In both cases, the imposed transition front and that inferred from the experimental measurements are also shown. These plots confirm the dominance of TS-instability in the vicinity of the windward and leeward symmetry planes, with the peak *N*-factor values along both planes reaching values of nearly 8. Because the flow becomes two-dimensional within the symmetry planes, the crossflow instability in the adjacent regions of the model surface remains weak, and hence, the disturbance amplification is dominated by the TS waves. The transport-equation-based transition models like the Langtry-Menter model have encountered difficulties with accurately capturing the growth of TS waves in these regions [49]. The TS *N*-factor also reaches a value around 8 between $\emptyset = 130°$ and $150°$ for $x/L \in [0.2, 0.3]$, i.e., the region where the experiments indicated transition. In the remaining azimuthal regions, the TS *N*-factor reaches a value around 5 along the transition front in the experiment. The contours of the CF *N*-factor in Fig. 16(b) indicate peak values of around 5, for $\emptyset = 30°$ and $170°$ along the inferred transition front, indicating that it is likely an important contributor of instability in those regions.

To determine the transition front to be imposed during the next iteration, it is necessary to define a composite criterion that accounts for the *N*-factors for both TS and CF instabilities. Furthermore, this criterion is expected to depend on both the unsteady disturbance environment in the facility and the surface roughness on the model surface. Stock [48] defined a specific dual *N*-factor criterion for transition by analyzing the LST-based *N*-factor characteristics at different angles of attack. Given that the present computations are limited to a single flow condition, the task of defining a composite *N*-factor metric based on the PSE computations that would be applicable to a broader range of flow conditions was deferred to a follow-on work. Therefore, we limit ourselves to using a simple, but representative metric that is based on the *N*-factors for both TS and CF instabilities, namely, $N_{dual} = N_{TS} + N_{CF}$. A threshold value of $N_{dual} = 8$ was found to coincide well with the measured transition front, as can been seen from Fig 16(c).

The transition front identified using the aforementioned simple criterion was then imposed as the transition location for the next iteration of the CFD run, which resulted in the skin-friction contours that were shown as CFD iteration two in Fig. 14(b). The resulting baseflow was then used to carry out another round of stability analysis, and the results are shown in Fig. 17. Once again, the revised prediction for the transition front based on $N_{dual} = 8$ is quite similar to the front predicted during the previous iteration and also to the transition front inferred from the experiment. The only significant difference relative to the experimental transition front is that the newly predicted front near the windward plane ($\emptyset < 30°$) is somewhat upstream of both the previously predicted front and that from the experiment. Also, the dual *N*-factor contours upstream of the inferred transition front from the experiment appear very similar to those shown in Fig. 16(c), except for the deteriorated smoothness of the contours. The latter may indicate some issues with the quality of the automated *N*-factor computation and we are currently attempting to resolve this problem.

Overall, the results indicate that the predicted transition front and the skin-friction contours compare well with those from the experiments and that the computations are nearly converged after two iterations. However, additional iterations will be run to verify convergence of the process. Future work will include

computations at additional angles of attack so that a subset of the data can be used to define a more optimal dual *N*-factor criterion, with the remaining data used for a more comprehensive assessment of the prediction process.

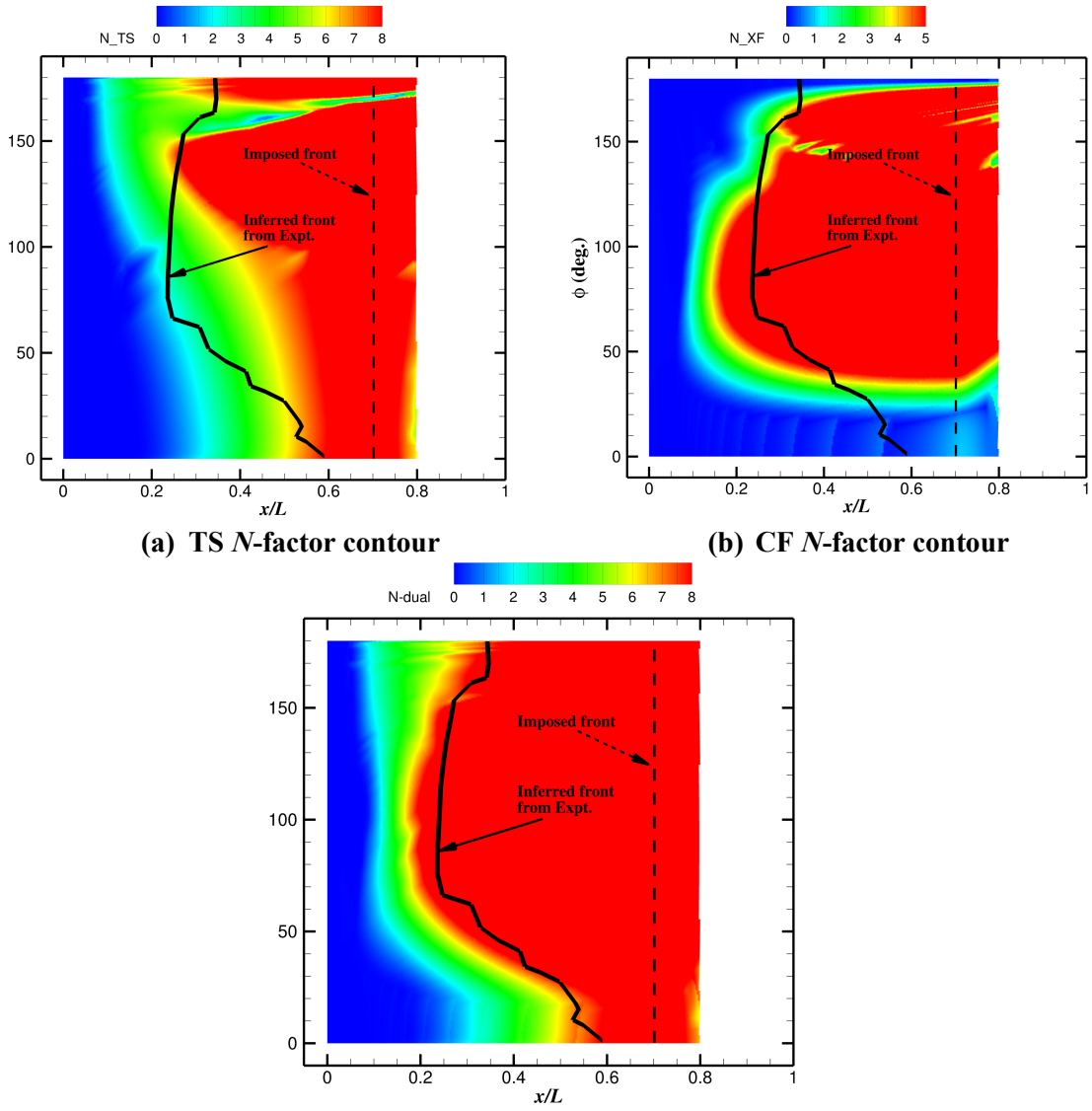

(a) TS *N*-factor contour **(b) CF *N*-factor contour**

(c) Dual *N*-factor contour

Fig. 16. *N*-factor contours obtained with PSE after the initial CFD run for the 6:1 prolate spheroid at $Re_L = 6.5 \times 10^6$ and $\alpha = 10°$. Indicated by dashed and solid lines are imposed transition front and the inferred transition front from the experiment.

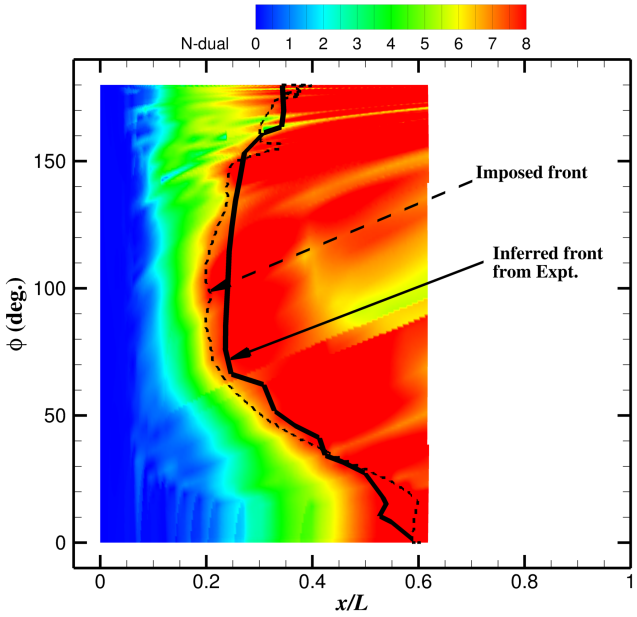

Fig. 17. Dual *N*-factor contours obtained with PSE after the second CFD run for the 6:1 prolate spheroid at $Re_L = 6.5 \times 10^6$ and $\alpha = 10°$. Indicated by dashed and solid lines are imposed transition front and the inferred transition front from the experiment.

E. NASA Juncture Flow Model with a Symmetric Wing

The final test case chosen for the assessment of the automated CFD-integrated transition prediction tool suite involves a civil transport configuration based on a new NASA juncture flow experiment that was recently tested in the NASA Langley 14- by 22-Foot Subsonic Tunnel. The original NASA juncture flow experiment [50-53] was carried out at NASA Langley between late 2017 and Spring 2020. It had the aim of supporting the assessment, validation, and improvements to CFD turbulence models by providing flow-field data for the separated flow near the wing-juncture trailing-edge region, along with quantified boundary conditions, geometry, and measurement uncertainties. The recently completed juncture flow experiment has a slightly different configuration from the previous campaign in that the wing has a symmetric cross-section such that a part of the wing section is based on the NACA 0015 airfoil. The symmetric wing configuration is expected to yield a much smaller separation than the F6-based wing used in the earlier campaign, hence providing data for evaluating the ability of the CFD model to make accurate predictions of incipient separation [51]. Additionally, a side goal of the experimental campaign was to use IR thermography to measure the transition location on the untripped swept wing over a range of angles of attack. Therefore, this new series of experiments should help the assessment of both RANS turbulence models and transition prediction models based on stability theory or RANS-like, phenomenological transport equations.

The model is a full-span, wing-fuselage body and has the same fuselage as that used in the previous experimental campaign with a nominal length of 4839±2 mm. The top-bottom symmetric wing has a wingspan (tip-to-tip) of 3327±2 mm, has no dihedral, and also includes an inboard, leading-edge horn. The crank chord was 581±1 mm and the leading-edge wing sweep was approximately 37.3 degrees. All the tests are being carried out at the NASA Langley 14- by 22-Foot Subsonic Tunnel, which is a closed-circuit atmospheric-pressure wind tunnel, with the crank chord-based Reynolds number expected to be fixed at 2.4 million throughout the tests. More details on the model geometry and about the experiments can be found on the NASA Juncture Flow website.[‡‡]

The flow condition reported in this work corresponds to a freestream temperature of 288.84 K, Mach number of 0.189, a Reynolds number based on the crank chord equal to 2.4×10^6, and 5° angle of attack. The free stream turbulence intensity (FSTI) was prescribed to be 0.08% based on previous characterization of the tunnel [54], and the surface roughness of the model was specified to be 3.3 μm based on the roughness levels

[‡‡] https://turbmodels.larc.nasa.gov/Other_exp_Data/JunctureFlow_0015/junctureflow_0015_exp.html

generally seen on a painted surface [55]. The results shown here were also included as part of an earlier report [56] and additional details can be found there.

While the original model is full span, the computation was carried out for a semispan geometry under the assumption of symmetry across the x-z plane. The baseline mesh for the semispan geometry used in these computations had seven overset near-body blocks (three on the fuselage, including its nose and tail, one wing-body collar grid, and three on the wing, including its tip). The generation of off-body grids and hole cutting were carried out by using OVERFLOW's domain connectivity function (DCF) approach. The wing and fuselage near-body grids had 325 points in the wall-normal direction with a near-wall spacing of 2.6 x 10^{-3} mm ($y+ \sim 0.5$, based on the midchord location), a growth rate of 1.02, around 150 points within two boundary layer thickness distance, and the initial 10 grid points near the wall being uniformly spaced. It also contained 433 points around the wing in the chordwise direction (25 points in the trailing edge) and 463 points in the spanwise direction. The near-body grid had an overall grid count of approximately 140 million points. The far-field boundaries of the outer-body grids were placed at approximately 100 crank chords.

The mean flow computation at the desired flow condition was carried out by using the Spalart-Allmaras RANS model with rotation-curvature correction (RC) [57], quadratic constitutive relation (QCR2000) [58], and an imposed transition front on both sides of the wing. The initial transition front was specified to obtain the maximum extent of laminar flow without any flow separation. This can be achieved by either running the flow under laminar assumption and setting the transition location upstream of where separation occurred or by using the pressure distribution obtained from a fully turbulent simulation and setting the transition front as far downstream as possible from the suction peak while not producing any separation. As in the case of the prolate spheroid, no intermittency distribution function was used due to ambiguities regarding how it should be formulated for a case where both TS and CF instabilities contribute to the transition process. The fuselage itself was run fully turbulent, letting the RANS model numerically transition from laminar-to-turbulent without specifying any trip locations.

The contours of the pressure coefficient over the semispan juncture flow model with the top-down symmetric wing are shown in Fig. 18. These contours are based on the computation with an imposed transition front. In general, the suction peak on the upper surface of the wing occurs relatively close to the leading edge and the aft portion of the wing has an adverse streamwise pressure gradient. Therefore, the boundary layer flow over a majority of the upper surface was expected to be turbulent. On the lower surface of the wing, all the spanwise locations experience a region of acceleration followed by a region of weak adverse pressure gradient. See Ref. [56] for additional details.

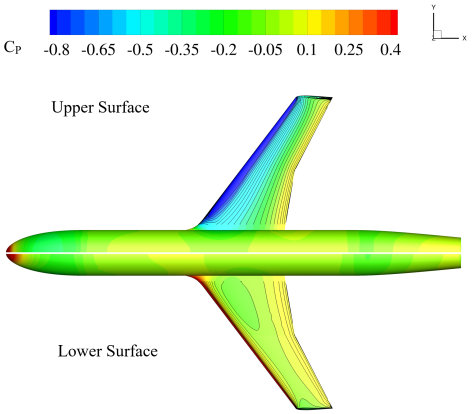

Fig. 18. Surface pressure distribution contours on the juncture flow model with top-bottom symmetric wing for $\alpha = 5$ (based on maximum laminar mean flow). The contour lines are also shown on the wing portion.

The contours of N_{TS} and N_{CF} within the laminar region of the solutions for $\alpha = 5°$, and on both the upper and the lower surfaces of the wing obtained with the nonorthogonal PSE are shown in Fig. 19. The PSE analysis was carried out using streamlines generated from approximately 50 seed points, uniformly distributed across the span of the wing. The inboard region of the lower surface of the wing indicates a region of large N_{CF} values, signifying significant stationary crossflow effects. There is a small region on the inboard portion of the wing, $0.4\text{ m} < y < 0.8\text{ m}$ and $x > 2.6\text{ m}$, with large values of both N_{TS} and N_{CF} (see Fig.

19(b)), indicating comparable levels of amplification for both types of instability within this region. On the other hand, the TS instability remains dominant on the upper surface of the wing and the location at which $N_{TS} \approx 8$ is close to the leading edge throughout the model span, with the contour lines for N_{TS} remaining parallel to the leading edge. The lack of a significant crossflow instability on the upper surface of the wing could be attributed to the rapid acceleration near the leading edge, which is then followed by an adverse pressure gradient. Following the results of transition analysis for the transonic wing-body combination known as the CRM-NLF [59], we use a dual $N_{TS} - N_{CF}$ criterion that is defined as:

$$N_{dual} = \left(\frac{N_{TS}}{N_{TS,c}}\right)^{a_{TS}} + \left(\frac{N_{CF}}{N_{CF,c}}\right)^{a_{CF}} \tag{9}$$

where the subscript c refers to the critical value, and the exponents a_{TS} and a_{CF} control the level of interaction between the two types of instability waves can be used to identify the overall transition front for this case. The critical N_{TS} and N_{CF} are set to 8, based on the disturbance level in the wind tunnel and the assumed roughness level of the model, along with $a_{TS} = 3$ and $a_{CF} = 3$. A threshold value of $N_{dual} = 1$ was expected to provide a good indication of the transition location. The predicted transition location obtained by using these values in Eq. 9 is shown Fig. 20 for both the suction and pressure surfaces of the wing, along with the predictions based on the LM2015 model (which corresponds to a modification of the LM2009 model to account for stationary crossflow effects). On the upper surface of the wing, with TS being the dominant instability mode, the front predicted by the transition model appears to closely match that from the stability analysis. On the lower surface of the wing, the predicted fronts from LM2015 also closely match those from stability analysis in most parts of the wing, except around the break and selected portions in the inboard portion of the wing. The general agreement between the prediction based on stability analysis and that from the transport-equation-based transition model provides confirmation that the integrated transition prediction process (including the definition of the dual *N*-factor) is working as intended. However, unlike the previous cases, we have not converged the iterative computation of the transition process. Thus, additional computations will be performed in future to confirm that convergence is achieved within a few additional cycles of the CFD run and stability analysis. When IR thermography images become available from the ongoing experiment, we will be able to verify how accurate these results are qualitatively.

IV. Concluding Remarks

Applications of transport-equation-based transition models that can be embedded into a RANS framework have gained substantial ground in recent years, due to both the ease of integration into existing parallel CFD codes and the ease of application to complex flow geometries. Yet, their accuracy remains a weak link as they do not account for much of the transition physics by virtue of being based on empirical correlations derived via limited data from low-speed experiments. On the other hand, linear stability methods have an advantage through their relationship to an important piece of the transition physics but are often difficult to integrate into existing CFD codes and, furthermore, require a significant degree of user expertise. Recent years have witnessed significant progress in terms of addressing those challenges in integrating stability-analysis-based transition prediction with CFD solvers. However, those capabilities have been code specific in general. Despite the range of CFD tools available both within NASA (including but not limited to DPLR, FUN3D, LAURA, LAVA, OVERFLOW, USM3D, VULCAN-CFD, and WIND), and the several unique capabilities of those codes, they have lacked such integration until now. The goal of this work has been to utilize the recently enhanced capabilities of the NASA stability analysis software suite LASTRAC to perform stability analysis for partly laminar flow solutions from both structured and unstructured grids toward the development of a tool suite for an automated, CFD-integrated modeling of the transition process. In principle, this tool suite would be easily extensible to either of the available CFD codes via a common interface to the LASTARC code. An initial implementation of this type for the FUN3D code was presented in a preceding work by Hildebrand et al. [28]. In the present work, we extend that capability to test and demonstrate an automated, CFD-integrated transition prediction process that is based on a loose coupling of the LASTRAC stability analysis tool with the structured, overset-grid compatible OVERFLOW CFD solver. We emphasize that the goal of complete automation is yet to be achieved and that additional work is needed to improve the robustness and achieve more thorough automation. The present work amounts to a progress report on the ongoing effort toward achieving that goal. As an initial assessment, we have presented the

results of applying the current toolset to simple, 2D canonical cases such as the flat plate and an NLF-0416 airfoil, as well as fully 3D configurations such as the prolate spheroid and the NASA juncture flow model involving a wing based on a symmetric airfoil contour.

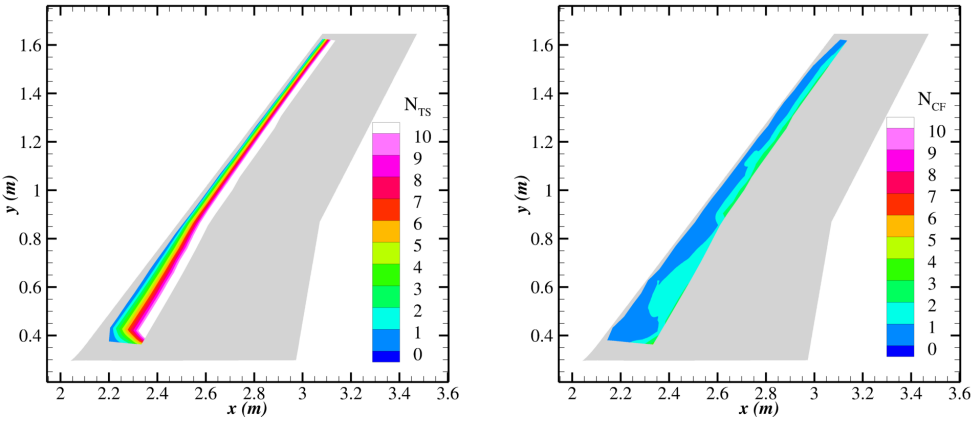

(a) Upper surface

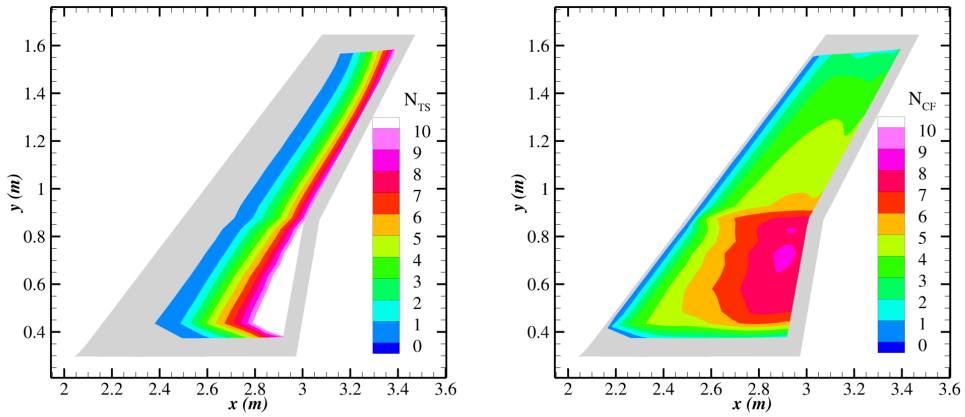

(b) Lower surface

Fig. 19. *N*-factor contours of TS waves ($\beta = 0$) and stationary CF waves ($f = 0$) calculated with nonorthogonal PSE for $\alpha = 5°$.

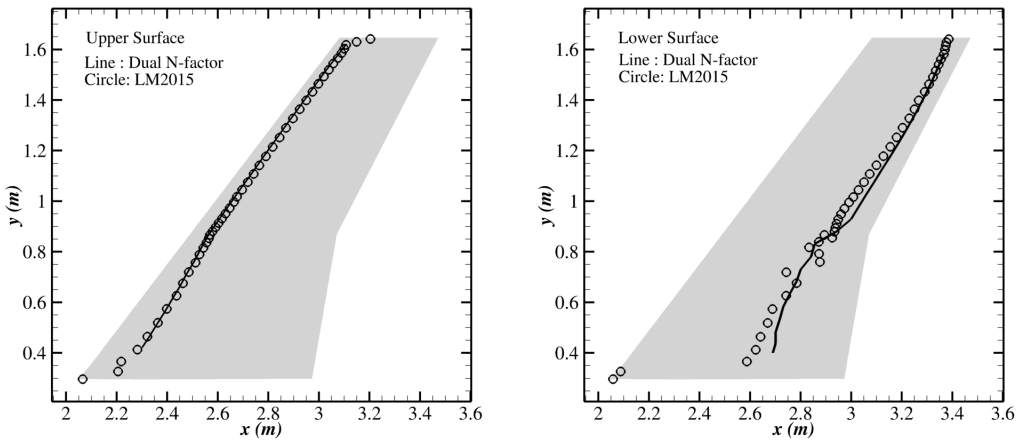

Fig. 20. Transition fronts on the upper and lower surfaces of the top-bottom symmetric wing of the juncture flow model, as predicted by the stability analysis and the LM2015 model, respectively.

The flat plate configuration was tested under a range of sufficiently low freestream turbulence levels, using the extensive available data to assess the accuracy of the integrated prediction process. Availability of data regarding the transition zone for this case also allowed for the calibration and assessment of the intermittency distribution function that is designed to allow a smoother evolution of the laminar flow into the turbulent flow. The incorporation of the intermittency function enhances the robustness of the iterative convergence process and should also provide more accurate estimates of the transition zone length, and hence, the integrated drag coefficient. The results from the integrated prediction tool compared reasonably well with the data from the experiments and the automated process achieved iterative convergence within four outer iterations of the cycle consisting of a CFD run followed by stability analysis.

The NLF-0416 airfoil was tested under conditions of two different Reynolds numbers and angles of attack, allowing for transition scenarios involving both TS-instabilities as well as that induced by a laminar separation bubble. This test case also allowed us to assess the robustness of the predicted solution to the choice of initial transition location as part of the input parameters provided by the user. The results demonstrated that the automated process is able to recover even when the initial transition location is specified far upstream of the actual transition location and achieves convergence within four or five cycles at most. The predicted results closely matched the available data from experiments as well as the predictions based on LM2009 and AFT transition models. The same intermittency function that was used in the case of flat plate was also applied here. However, given the possibility of a different transition scenario involving the separation bubble, alternate definitions of the transition zone length need to be explored and assessed. Such an effort is likely to lead to a more broadly applicable formulation of the intermittency function and also help with transition modeling for more complex 3D cases.

The 6:1 prolate spheroid at $\alpha = 10°$ was used to demonstrate the ability of the method to use a simplified dual *N*-factor criterion for predicting transition scenarios involving a combination of both TS and CF instabilities. While only two iterations of the prediction cycle were performed for this case, the results indicate near-convergence and a good match against the experimental data. Additional iterations are in progress to verify the convergence of the iterative process.

Finally, computations were performed for a wing-body combination model (namely, the juncture flow model with top-bottom symmetric wing) that was used in wind tunnel tests at the NASA Langley Research Center in 2022. These computations involved a crank chord-based Reynolds number of 2.4 million and an angle of attack equal to $\alpha = 5°$, and were intended as a test for the applicability of the developed tool to complex geometries relevant to aeronautical applications. Unlike the previous cases, only one iteration of the coupled solver was run due to time constraints. Similar to the prolate spheroid case, both TS and CF instabilities come into play on different portions of the wing and the pretest predictions from the initial run of the integrated stability analysis tool matched well with those obtained using the LM2015 model that is expected to work well for this low-speed configuration. Additional iterations of the coupled solver are planned for and will be included in a future publication. The accuracy of these results can be further assessed when data from the recently concluded experiment becomes available. For both 3D cases reported here, no

intermittency distribution function was used due to a lack of information about the transition zone for cases involving both TS and CF instabilities.

One of the major omissions from this paper pertains to performance comparisons highlighting the time-to-solution aspects of the integrated approach *vis-a-vis* the RANS-based transition models. We deemed it appropriate to defer such comparisons until after the workflow has been optimized and best practices have been identified. Also, flow configurations involving transonic conditions and the potential presence of a shock system will bring in additional transition scenarios and those, too, will be addressed in future work.

One significant bottleneck regarding the application of a stability-coupled computation of boundary-layer transition is the need for well-resolved boundary layer profiles in the laminar parts of the mean-flow computations which could lead to significant increase in computational costs and affect convergence, especially in the context of complex 3D geometries. As part of PyLASTRAC development, a deep learning model [26] was developed to perform intelligent interpolation of underresolved boundary layer onto a more well-defined set of points across the boundary layer to carry out an accurate stability analysis. Such an approach could significantly reduce the gridding requirements to be on par with regular RANS computations. This technique will be further explored in our upcoming research efforts. Furthermore, significant additional developments are still necessary to achieve a tool suite that can be deployed in more routine CFD applications. One such enhancement that would benefit all CFD solvers is to improve the robustness of the hands-off stability computation.

In the narrower context of the OVERFLOW solver, we note that the current PyLASTRAC capability to convert the CFD solution to a LASTRAC compatible mean flow is based on translating the CFD mean flow to an unstructured fully tetrahedral grid solution format. This is easily achieved for either purely unstructured grid solution or for point-matched multiblock structured grids. However, an overset grid setting often involves multiple regions that are not perfectly matched across the regions of grid overlap. In such scenarios, one must honor any I-blanking, donor-receptor relationships, and generate a LASTRAC compatible mean flow based on a unique set of grid points and the corresponding values of solution variables. Development of this capability is part of our ongoing work. Finally, we note that the present framework also allows an easy replacement of the transition solver process based on the stability code to that using a reduced order model, based on either curve fits or deep learning algorithms. The outcomes of our preliminary efforts on the latter front have been promising, indicating a higher robustness to the quality and resolution of the mean boundary layer profiles. Therefore, we also plan to integrate those models into the present tool as a more efficient alternative to the actual stability computation.

Acknowledgments

This research is sponsored by the NASA Transformational Tools and Technologies (TTT) project of the Transformative Aeronautics Concepts Program under the Aeronautics Research Mission Directorate. The research of Balaji Venkatachari is funded by the NASA Langley Research Center through the cooperative agreement 2A00 (Activity 201133) with the National Institute of Aerospace (NIA). The authors thank Joseph Derlaga and Pieter Buning of NASA Langley Research Center for their help with the use of OVERFLOW and many other useful discussions. The authors would also like to acknowledge Pedro Paredes of NIA for his help and valuable suggestions.

References

[1] Slotnick, J., Khodahoust, A., Alonso, J., Darmofal, D., Gropp, W., and Mavriplis, D., "CFD Vision 2030 Study: A Path to Revolutionary Computational Aerosciences," NASA/CR-2014-218178, 2014.

[2] Warren, E. S., and Hassan, H. A., "Transition Closure Model for Predicting Transition Onset," *Journal of Aircraft*, Vol. 35, No. 5, September- October 1998, pp. 769-775.

[3] Walters, D. K., and Leylek, J. H., "A New Model for Boundary-Layer Transition Using a Single-Point RANS Approach," *ASME J. of Turbomach*, Vol. 126(1), 2004, pp. 193–202.

[4] Langtry, R. B., and Menter, F. R., "Correlation-Based Transition Modeling for Unstructured Parallelized Computational Fluid Dynamics Codes," *AIAA Journal*, Vol. 47, No. 12, 2009, pp.2894–2906.

[5] Medida, S., and Baeder, J., "Application of the Correlation-based the γ-Re$_{\theta t}$ Transition Model to the Spalart-Allmaras Turbulence Model", AIAA Paper 2011-3979, 2011.

[6] Langtry, R. B., Sengupta, K., Yeh, D. T., and Dorgan, A. J., "Extending the γ-Re$_{\theta t}$Correlation based Transition Model for Crossflow Effects," AIAA Paper 2015-2474, 2015.
[7] Fu, S., Wang, L., "RANS modeling of High-Speed Aerodynamic Flow Transition with Consideration of Stability Theory", *Progress in Aerospace Sciences*, Vol. 58, 2013, pp. 36-59.
[8] Coder, J.G., and Maughmer, M.D., "Computational Fluid Dynamics Compatible Transition Modeling Using an Amplification Factor Transport Equation," *AIAA Journal*, Vol. 52, No. 11, 2014, pp.2506–2512.
[9] Coder, J.G., "Further Development of the Amplification Factor Transport Transition Model for Aerodynamic Flows," AIAA Paper 2019-0039, 2019.
[10] Smith, A. M. O., and Gamberoni, N., "Transition, Pressure Gradient and Stability Theory," Douglas Aircraft Company, Long Beach, Calif. Rep. ES 26338, 1956.
[11] van Ingen, J. L., "A Suggested Semi-Empirical Method for the Calculation of the Boundary Layer Transition Region," University of Delft, Dept. of Aerospace Engineering, Delft, The Netherlands, Rep. VTH-74, 1956.
[12] Herbert, T., "Parabolized Stability Equations," *Annu. Rev. Fluid Mech.,* 29:245-283, 1997.
[13] Stock, H. W., and Haase, W., "Navier-Stokes Airfoil Computations with e^N Transition Prediction Including Transitional Flow Regions," *AIAA Journal,* Vol. 38, No. 11, 2000, pp. 2059–2066.
[14] Drela, M. and Giles, M. B., "Viscous-Inviscid Analysis of Transonic and Low Reynolds Number Airfoils," *AIAA Journal*, Vol. 25, No. 10, 1987, pp. 1347–1355.
[15] Sturdza, P., "An Aerodynamic Design Method for Supersonic Natural Laminar Flow Aircraft," Ph.D. Thesis, Stanford University, California, USA, 2003.
[16] Davis, M. B., Reed, H. L., Youngren, H., Smith, B., and Bender, E., "Transition Prediction Method Review Summary for the Rapid Assessment Tool for Transition Prediction (RATTraP)," Technical Report AFRL-VA-WP-TR-2005-3130, Air Force Research Lab, Wright-Patterson AFB, OH, 2005.
[17] Cliquet, J., Houdeville, R., and Arnal, D., "Application of Laminar-Turbulent Transition Criteria in Navier-Stokes Computations," *AIAA Journal*, Vol. 46, No. 5, 2008, pp. 1182-1190.
[18] Campbell, R., Campbell, M., and Streit, T., "Progress Toward Efficient Laminar Flow Analysis and Design", AIAA 2011-3527.
[19] Perraud, J., Arnal, D., Casalis, G., Archambaud, J.-P., and Donelli, R., "Automatic Transition Predictions Using Simplified Methods," *AIAA Journal*, Vol.47, No. 11, 2009, pp. 2676-2684.
[20] Krumbein, A., Krimmelbein, N., and Schrauf, G., "Automatic Transition Prediction in a Hybrid Flow Solver – Part 1: Methodology and Sensitivities", *Journal of Aircraft*, Vol. 46, No. 4, 2009, pp. 1176 – 1190.
[21] Krumbein, A., Krimmelbein, N., and Grabe, C., "Streamline-Based Transition Prediction Techniques in an Unstructured Computational Fluid Dynamics Code", *AIAA Journal*, Vol. 55, No. 5, 2017, pp. 1548–1564.
[22] Shi, Y., Mader, C. A., He, S., Halila, G. L. O., and Martins, J. R. R. A., "Natural Laminar-Flow Airfoil Optimization Design Using a Discrete Adjoint Approach," *AIAA Journal*, Vol. 58, No. 11, 2020, pp.4702–4722.
[23] Halila, G. L. O., Fidkowski, K. J., Martins, J. R. R. A., "Toward Automatic Parabolized Stability Equation-Based Transition-to-Turbulence Prediction for Aerodynamic Flows," *AIAA Journal*, Vol. 59, No. 2, 2020, pp. 462–473.
[24] Chang, C.-L., "LASTRAC.3d: Transition Prediction in 3D Boundary Layers," AIAA Paper 2004-2542, 2004.
[25] Chang, C.-L., "Langley Stability and Transition Analysis Code (LASTRAC) Version 1.2 User Manual," NASA TM-2004-213233, 2004.
[26] Chang, C.-L., "Development of Physics-Based Transition Models for Unstructured-Mesh CFD Codes using Deep Learning Models," AIAA Paper 2021-2828, 2021.
[27] Nichols, R. H, and Buning, P. G., "User's Manual for OVERFLOW 2.3, Version 2.3," NASA Langley Research Center, Hampton, VA, Oct 2019. URL: https://overflow.larc.nasa.gov/users-manual-for-overflow-2-3/?doing_wp_cron=1650927883.9462668895721435546875 (accessed 25April,2022).
[28] Hildebrand, N., Chang, C.-L., Choudhari, M., Li, F., Venkatachari, B., and Paredes, P., "Coupling of the FUN3D Unstructured Flow Solver and the LASTRAC Stability Code to Model Transition," AIAA Paper 2022-1952, 2022.
[29] Paredes, P., Venkatachari, B., Choudhari, M., Li, F., Chang, C.-L., Zafar, M. I., and Xiao, H., "Toward a Practical Method for Hypersonic Transition Prediction Based on Stability Correlations," *AIAA Journal.,* Vol. 58, No. 10, 2020, pp. 4475–4484.
[30] Zafar, M., Choudhari, M., Paredes, P., and Xiao, H., "Recurrent Neural Network for End-to-End Modeling of Laminar-Turbulent Transition," *Data -Centric Engineering,* Vol. 2, 2021, E17:1–32.
[31] Narasimha, R., "The Laminar-Turbulent Transition Zone in the Boundary Layer," *Progress In Aerospace Sciences.*, Vol. 22, 1985, pp. 29–80.
[32] Narasimha, R., "Modeling the Transitional Boundary Layer," NASA CR-187487, 1990.
[33] Narasimha, R., and Dey, J., "Transition-Zone Models for 2-Dimensional Boundary Layers: A Review," *Sãdhanã*, Vol. 14, Part .2, 1989, pp. 93–120.
[34] Dhawan, S., and Narasimha, R., "Some Properties of Boundary Layer Flow during the Transition from Laminar to Turbulent Motion," *Journal of Fluid Mechanics*, Vol. 3, No. 4, 1958, pp. 418–436.
[35] Arnal, D., "Three-Dimensional Boundary Layers: Laminar-Turbulent Transition," AGARD-FDP-VKI Special Course, 1986.
[36] Solomon, W. J., Walker, G. J., and Gostelow, J. P., "Transition Length Prediction for Flows with Rapidly Changing Pressure Gradients," *Journal of Turbomachinery*, Vol. 118, No. 4s, 1986, pp. 744–751.

[37] Roe, P. L., "Approximate Riemann Solvers, Parameter Vectors, and Difference Schemes," *J. Comput. Phys.,* Vol. 43, No. 2, 1981, pp. 357–372.
[38] Nichols, R. H., Tramel, R. W., and Buning, P. G., "Solver and Turbulence Model Upgrades to OVERFLOW 2 for Unsteady and High-Speed Applications," AIAA Paper 2006-2824, 2006.
[39] Derlaga, J. M., Jackson, C. W., and Buning, P. G., "Recent Progress in OVERFLOW Convergence Improvements," AIAA Paper 2020-1045, 2022.
[40] Schubauer, G. B., and Skramstadt, H. K., "Laminar Boundary Layer Oscillations and Stability of Laminar Flow," *J. Aero. Sci.*, Vol. 14, No. 2, 1947, pp. 69–78.
[41] Schubauer, G. B., and Klebanoff, P. S., "Contribution on the Mechanics of Boundary Layer Transition," NACA-TR-1289, 1955, pp. 853–863.
[42] Savill, A. M., "Some Recent Progress in the Turbulence Modeling of By-Pass Transition," *Near-Wall Turbulent Flows*, edited by R. M. C. So, C. G. Speziale, and B. E. Launder, Elsevier, New York, 1993, p. 829.
[43] Crouch, J. D., "Instabilities in Boundary-Layer Flows and their Role in Engineering," *Proceedings of the IUTAM Symposium on One Hundred Years of Boundary Layer Research*, edited by G. E. A. Meier and K. R. Sreenivasan, Springer, Netherlands, 2006, p. 105.
[44] Dryden, H.L. "Airflow in the Boundary Layer near a Flat Plate," NACA Rep. 562, 1936.
[45] Somers D. M., "Design and Experimental Results for a Natural Laminar Flow Airfoil for General Aviation Applications," NASA TP-1861, 1981.
[46] Kreplin, H.-P., Vollmers, H., and Meier, H. U., "Wall Shear Stress Measurements on an Inclined Prolate Spheroid in the DFVLR 3M × 3M Low Speed Wind Tunnel, Göttingen," Data Report IB 222-84 A 33, DFVLR – Deutsche Forschungsund Versuchsanstaltfür Luftund Raumfahrt, DFVLR-AVA, 1985.
[47] Spall, R. E., and Malik, M. R., "Linear Stability of Three-Dimensional Boundary Layers over Axisymmetric Bodies at Incidence," *AIAA Journal*, Vol. 30, No. 4, 1992, pp. 905–913.
[48] Stock, H.W., "Infinite Swept-Wing Navier-Stokes Computations with e*N* Transition Prediction," *AIAA Journal*, Vol. 43, No. 6, 2005, pp.1221–1229.
[49] Krimmelbein, N.,and Krumbein, A., "Validation of Transition Modeling Techniques for a Simplified Fuselage Configuration," *Aerospace Science and Technology*, Vol. 118, 2021, pp. 107043.
[50] Rumsey, C., Neuhart, D., and Kegerise, M., "The NASA Juncture Flow Experiment: Goals, Progress, and Preliminary Testing," AIAA Paper 2016–1557, 2016.
[51] Kegerise, M. A. and Neuhart, D. H., "Wind Tunnel Test of a Risk-Reduction Wing/Fuselage Model to Examine Juncture-Flow Phenomena," NASA TM–219348, November 2016, https://ntrs.nasa.gov/archive/nasa/casi.ntrs.nasa.gov/20160014854.pdf.
[52] Rumsey, C. L., "The NASA Juncture Flow Test as a Model for Effective CFD/Experimental Collaboration," AIAA Paper 2018-3319, 2018.
[53] Kegerise, M. A. and Neuhart, D. H., "An Experimental Investigation of a Wing-Fuselage Junction Model in the NASA Langley 14- by 22-Foot Subsonic Tunnel," NASA TM–2019-220286, June 2019, https://ntrs.nasa.gov/archive/nasa/casi.ntrs.nasa.gov/ 20190027403.pdf.
[54] Neuhart, D. H., and McGinley, C. B., "Free-Stream Turbulence Intensity in the Langley 14- by 22-Foot Subsonic Tunnel," NASA TP 213247, August 2004.
[55] Dagenhart, J. R., Saric, W. S., Mousseux, M. C., and Stack, J. P., "Crossflow-Vortex Instability and Transition on a 45-Degree Swept Wing," AIAA Paper 89-1892, 1989.
[56] Venkatachari, B., Paredes, P., Choudhari, M. M., Li, F., and Chang, C.-L., "Pretest Computational Assessment of Boundary Layer Transition in the NASA Juncture Flow Model with an NACA 0015-Based Wing," AIAA Paper 2021-2502, 2021.
[57] Shur, M. L., Strelets, M. K., Travin, A. K., and Spalart, P. R., "Turbulence Modeling in Rotating and Curved Channels: Assessing the Spalart-Shur Correction," *AIAA Journal*, Vol. 38, No. 5, 2000, pp. 784–792.
[58] Spalart, P. R., "Strategies for Turbulence Modelling and Simulation," *International Journal of Heat and Fluid Flow*, Vol. 21, 2000, pp. 252–263.
[59] Paredes, P., Venkatachari, B., Choudhari, M. M., Li, F., Hildebrand, N., and Chang, C.-L., "Transition Analysis for the CRM-NLF Wind Tunnel Configuration," AIAA Paper 2021-1431, 2021.